Monthly Notices of the ROYAL ASTRONOMICAL SOCIETY

MNRAS **544,** 95–112 (2025) https://doi.org/10.1093/mnras/staf1668
Advance Access publication 2025 October 1

Ion-neutral chemistry at icy moons: the case of Ganymede

A. Beth [1]★ M. Galand [1] X. Jia [2] and F. Leblanc [3]

[1] *Imperial College London, Department of Physics, London, SW7 2AZ, UK*
[2] *University of Michigan, Department of Climate and Space Sciences and Engineering, Ann Arbor, MI 48109-2143, USA*
[3] *LATMOS/IPSL, Sorbonne Université, UVSQ, CNRS, Paris, 75252, France*

Accepted 2025 September 23. Received 2025 September 23; in original form 2025 June 10

ABSTRACT

Icy moons orbiting giant planets are often described as airless bodies though they host an exosphere where collisions between neutral species are scarce. In the case of Ganymede, the neutral composition is dominated by H_2O, H_2, and O_2. Past observations by Galileo showed that Ganymede hosts an ionosphere and those by Juno revealed the presence of H_3^+, an ion species only stemming from ion-neutral collisions. H_3^+ detection suggests that ions and neutrals might still collide and be the source of new ion species on icy moons. We examine Ganymede's ability to host a more diverse ionosphere in terms of ion composition than previously thought and predict its variety. We upgraded our test-particle code of Ganymede's ionosphere, formerly collisionless, to include ion-neutral collisions in a probabilistic manner. The updated code is applied to three Galileo flybys of Ganymede that were investigated in the absence of chemistry. Both sets of simulations have been compared and the effect of ion-neutral chemistry has been assessed. We show that in the case of an exosphere predominantly composed of H_2O, H_2, and O_2, the ionosphere is made not only of their associated cations but also of H_3^+, H_3O^+, and O_2H^+. Simulations reveal that, depending on the location, the contribution of H_3^+ and H_3O^+ to the ion composition may be significant. Strong dayside/nightside and Jovian/anti-Jovian asymmetries in the ion composition are identified. Our findings are key to interpreting Juno and future JUICE ion mass spectrometer data sets.

Key words: MHD – plasmas – methods: numerical – planets and satellites: atmospheres – planets and satellites: individual: Ganymede.

1 INTRODUCTION

Ganymede is the largest moon in the Solar system. Amongst its uncommon characteristics, such as bearing an intrinsic magnetic field (M. G. Kivelson et al. 1996) and a potential subsurface ocean (M. Kivelson, K. Khurana & M. Volwerk 2002; J. Saur et al. 2015), Ganymede is surrounded by a thin, almost collisionless layer of gas so-called exosphere. This layer of gas is produced through several main processes: sublimation of water ice, sputtering by the harsh Jovian magnetospheric environment (C. Plainaki et al. 2015; A. Pontoni et al. 2022) and ionospheric ions (G. Carnielli et al. 2020b), and radiolysis (R. E. Johnson 1990; M. Marconi 2007; V. I. Shematovich 2016) leading to an exosphere dominated by H_2O, O_2, and H_2, in part supported by remote-sensing observations (e.g. C. A. Barth et al. 1997; D. T. Hall et al. 1998; L. Roth et al. 2021, 2023). In addition, there was recent evidence for a local CO_2 gas patch over the leading side of the North polar cap (D. Bockelée-Morvan et al. 2024).

The transition from collisional to collisionless environments is defined as the exobase where the scale height of the different neutral species is of the order of the mean free path. In the case of Ganymede, the exobase remains close to the surface except near the subsolar point where sublimation drastically increases the number density of H_2O, reducing the mean free path of neutral species (M. Marconi 2007; F. Leblanc et al. 2017, 2023). However, Ganymede's atmosphere is often regarded as collisionless, hence models of its atmosphere neglect collisions if possible (e.g. A. Vorburger et al. 2022; F. Leblanc et al. 2023; A. Vorburger et al. 2024), allieviating computational resources.

By ionizing this exosphere, through photo- and electron-impact ionization, Ganymede hosts an ionosphere as well, that has been probed *in situ* by several flybys of the Galileo spacecraft (A. Eviatar, V. M. Vasyliūnas & D. A. Gurnett 2001; A. Beth et al. 2025) and recently by the Juno spacecraft (W. S. Kurth et al. 2022). As the spacecraft approached the moon, the plasma density probed *in situ* via the PWS instrument (D. A. Gurnett et al. 1992) increased, reaching 200 cm^{-3} for the G02 flyby at closest approach. Although Galileo did not offer us the ability to infer the ion composition during these flybys, preliminary collisionless modelling that combines DSMC simulations of the exosphere (F. Leblanc et al. 2017, 2023) and MHD simulations of Ganymede's electromagnetic environments (X. Jia et al. 2008, 2009) showed evidence for an ionosphere mainly made of H_2^+ and O_2^+ ions (G. Carnielli et al. 2019) that agree with the *in situ* total plasma number density for some flybys (A. Beth et al. 2025). There is good agreement in terms of ion energy distribution and shape within the Alfvén wings between simulations and in-situ observations by PLS (L. A. Frank et al. 1992), but worse in terms of

★ E-mail: arnaud.beth@gmail.com

© The Author(s) 2025.
Published by Oxford University Press on behalf of Royal Astronomical Society. This is an Open Access article distributed under the terms of the Creative Commons Attribution License (https://creativecommons.org/licenses/by/4.0/), which permits unrestricted reuse, distribution, and reproduction in any medium, provided the original work is properly cited.

Downloaded from https://academic.oup.com/mnras/article/544/1/95/8269935 by Imperial College of Science Technology and Medicine user on 06 November 2025

absolute values, in part due to the lack of field-aligned electric fields in the modelling. In contrast to Galileo, thanks to its time-of-flight ion mass spectrometer, the Juno spacecraft provided further insight with the additional capability to separate masses. Not only were H_2^+ and O_2^+ indeed unambiguously identified, supporting early findings of G. Carnielli et al. (2019) and A. Beth et al. (2025), but also H_3^+ and water-group ions around 16 u q^{-1}, a priori dominated by O^+, were also detected (F. Allegrini et al. 2022; P. W. Valek et al. 2022).

The serendipitous detection of H_3^+ by Juno casts doubt on the 'collisionlessness' of Ganymede's exo-ionosphere. Indeed, H_3^+ cannot be produced through the ionization of a neutral species. It is primarily found in the interstellar medium and in the thermosphere of gas giants: H_3^+ is produced through ion-neutral chemistry, mainly $H_2 + H_2^+$. This implies that collisions between ion and neutral species may still happen at Ganymede. J. H. Waite Jr et al. (2024) attempted to model H_3^+, assuming photochemical equilibrium (neglecting transport but including dissociative recombination), imposing the electron density profile from D. R. Buccino et al. (2022), and applying a limited chemical network that does not account for all possible ion and neutral species.

Based on the neutral composition of Ganymede's exosphere and their ionized counterpart, three new ions species are produced through ion-neutral collisions only: H_3^+ (present around gas giants and in the interstellar medium), H_3O^+ (found at planets and comets), and O_2H^+ (not yet detected). In this paper, we address the ability of Ganymede, an icy moon, to host these additional ions, hence, a more diverse ionosphere than previously thought. By updating their test-particle model from A. Beth et al. (2025) to include ion-neutral collisions, we show that Ganymede's ionosphere for different configurations, corresponding to those of Galileo's flybys, is not only made of H_2^+, O_2^+, and H_2O^+ (along with H^+, O^+, and HO^+ to a lesser extent) but of H_3^+ and H_3O^+ (O_2H^+ found to be negligible).

We present the update made for the test-particle model to account for ion-neutral collisions in Section 2. The results are presented in Section 3, then discussed in Section 4, followed by the conclusions in Section 5.

2 METHOD

2.1 Model description

The present modelling work builds upon A. Beth et al. (2025), in which the test particle model is described in detail, including inputs and approach. We summarize here the main steps. First, we use the simulated neutral exospheric number densities of the different neutral species (H, H_2, O, HO, H_2O, O_2, ignoring CO_2 and its fragments that are not adequately modelled yet) as a function of the altitude from the surface to $5R_G$ (R_G: Ganymede's radius), of the different neutral species in the environment of Ganymede from a DSMC model (F. Leblanc et al. 2023). Secondly, we generate ions as macroparticles at a rate based on the ionization frequency, which includes both photo- and electron impact ionization (values are those from G. Carnielli et al. 2019). Once produced, macroparticles are transported through the magnetosphere via electric and magnetic fields. These are extracted from MHD simulations at Ganymede performed for the different Galileo flybys (X. Jia et al. 2008, 2009). Based on the time spent in the cells of our simulation grid, one can derive the moments, such as number densities and mean velocities of the different ion species within Ganymede's magnetosphere.

The gyrofrequency of the ion primarily governs the time-step in the simulation Δt. We have fixed $\Delta t[\mathrm{s}] = 10^{24} m_i[\mathrm{kg}] \approx 1.7 \times 10^{-3} m_i[\mathrm{u}]$ where m_i is the ion mass. The original limitation was to resolve at least 1/20 of the gyromotion for good accuracy with the Boris pusher (J. P. Boris 1970). At Ganymede, the strongest magnetic field is ∼1440 nT near the poles such that:

$$\Delta t < \min\left\{\frac{1}{20}\frac{2\pi}{\omega_{ci}}\right\} = \min\left\{\frac{1}{10}\frac{m_i\pi}{q_i B}\right\} = \frac{1}{10}\frac{m_i\pi}{q_i \max\{B\}} = 1.36 \times 10^{24} m_i \quad (1)$$

Δt must also be constrained by the grid resolution (i.e. fulfilling the Courant–Friedrich–Lewy (CFL) condition). As our grid resolution Δx is ~ 66 km and $\Delta t[s] \sim 0.0017 m_i$[u], the heaviest ion ($O_2^+$) would need to be faster than 10^3 km s^{-1} to break the CFL condition. That is almost an order of magnitude higher than the speed of the undisturbed Jovian plasma and three orders higher than that of the plasma flow near Ganymede's surface (A. Beth et al. 2025).

We assume that these ions have no feedback on the field: The MHD simulations are not self-consistent and are purely based on the interaction of the Jovian plasma with Ganymede's magnetic field. A. Beth et al. (2025) showed that the modelled number densities are still consistent with in-situ Galileo PWS observations for some Galileo flybys (e.g. G01 and G07), and the trends in the ion energy spectra seen with PLS are captured, while discrepancies persist. Their simulations were performed with the collisionless version of the test-particle model.

2.2 Implementation of collisions

Compared with the model of A. Beth et al. (2025), we have added ion-neutral collisions that macroparticles can undergo at each time-step while transported through the ionosphere. Initially, the trajectory of the macroparticle is simulated by applying the Boris scheme (J. P. Boris 1970). We interpolate the electric and magnetic fields at the location of the macroparticle and use them as input to update the particle's position and velocity from t to $t + \Delta t$. That is repeated until the ion crashes on to Ganymede's surface or leaves the simulation box (see Appendix B). In this updated version of the test-particle model, to account for ion-neutral collisions during the period $[t; t + \Delta t]$, we estimate the probability of colliding with a neutral species $p_{\mathrm{collision}}$ given by

$$p_{\mathrm{collision}} = 1 - \exp\left(-\sum_n \nu_{i,n}^{\mathrm{tot}} \Delta t\right) \quad (2)$$

$$\nu_{i,n}^{\mathrm{tot}} = n_n < \sigma_{i,n}^{\mathrm{tot}}(v_{\mathrm{rel.}}) v_{\mathrm{rel.}} > \quad (3)$$

where n_n is the number density of the neutral species n, $\sigma_{i,n}^{\mathrm{tot}}$ stands for the total collision cross-section between the ion species i and the neutral species n, $\nu_{i,n}$ is the collision frequency between both species and $< \sigma_{i,n}^{\mathrm{tot}}(v_{\mathrm{rel.}}) v_{\mathrm{rel.}} >$ is defined as

$$< \sigma_{i,n}^{\mathrm{tot}}(v_{\mathrm{rel.}}) v_{\mathrm{rel.}} > = \int_{\mathbb{R}^3} \sigma_{i,n}^{\mathrm{tot}}(v_{\mathrm{rel.}}) v_{\mathrm{rel.}} f_n(\vec{V})\, \mathrm{d}^3\vec{V}, \quad (4)$$

where f_n stands for the velocity distribution function of the targeted neutral and the relative speed $v_{\mathrm{rel.}} = \|\vec{v}_i - \vec{V}\|$ where $\vec{v}_i$ and $\vec{V}$ stand for the ion and neutral velocities, respectively. This represents the weighted/averaged rate at which an ion collides with neutrals following a velocity distribution function f_n. We have ignored the angular dependency of the cross-section for the sake of simplicity. In practice, f_n is assumed to be a normalized Maxwell–Boltzmann velocity distribution defined by a mean bulk velocity $\vec{V}_n$ and a temperature T_n. Still equation (4) remains impractical to solve. $< \sigma_{i,n}^{\mathrm{tot}}(v_{\mathrm{rel.}}) v_{\mathrm{rel.}} >$ can be approximated in two different ways. The first approach is to drop the integral and assume that all neutrals

Downloaded from https://academic.oup.com/mnras/article/544/1/95/8269935 by Imperial College of Science Technology and Medicine user on 06 November 2025

move at $\vec{V}_n$ such that

$$<\sigma_{i,n}^{\rm tot}(v_{\rm rel.})v_{\rm rel.}>\approx \sigma_{i,n}^{\rm tot}(\|\vec{v}_i-\vec{V}_n\|)\|\vec{v}_i-\vec{V}_n\|, \quad (5)$$

valid as long as $v_{\rm rel.}\approx\|\vec{v}_i-\vec{V}_n\|\gg v_{\rm th,n}$, where $v_{\rm th,n}=\sqrt{2k_BT_n/m_n}$ is the thermal speed of the neutral species n. In the limit $\|\vec{v}_i-\vec{V}_0\|\lesssim v_{\rm th,n}$, a more refined model would be needed to take into account the velocity dispersion of the neutrals. For instance, in the hard sphere approximation, one can evaluate (see e.g. H. Fahr & K. G. Müller 1967)

$$<\sigma_{i,n}^{\rm tot}(v_{\rm rel.})v_{\rm rel.}>\approx \sigma_{i,n}^{\rm tot}(\|\vec{v}_i-\vec{V}_n\|)\cdot \underbrace{v_{\rm th,n}\left[\frac{\exp(-x^2)}{\sqrt{\pi}}+x\left(1+\frac{1}{2x^2}\right)\mathrm{erf}(x)\right]}_{\int_{\mathbb{R}^3}\|\vec{v}_i-\vec{V}\|f_n(\vec{V})\,\mathrm{d}^3\vec{V}}, \quad (6)$$

where $x=\|\vec{v}_i-\vec{V}_n\|/v_{\rm th,n}$ (consistent with equation 6 for $x\gg1$). Nevertheless, equation (6) requires the full, exhaustive, and accurate knowledge of all $\sigma_{i,n}$ for all combinations $\{i,n\}$ and over a wide range of energy (that said $v_{\rm rel.}$) typically from 0.1 eV to 100–200 eV. That becomes unpractical as the number of neutral and ion species increases. It may significantly slow down the computation and increase the complexity of the model due to the large number of outcomes for all collisions. In addition, not all cross-sections between the different ions and neutrals are available.

The second approach to approximate equation (3) is

$$<\sigma_{i,n}^{\rm tot}(v_{\rm rel.})v_{\rm rel.}>=\int_{\mathbb{R}^3}\sigma_{i,n}^{\rm tot}(\vec{V})\|\vec{V}\|f_n(\vec{V})\,\mathrm{d}^3\vec{V}=k_{in}(T_n), \quad (7)$$

where $k_{in}(T_n)$ is the ion-neutral reaction rate coefficient. We have decided to use the second approach (see also the discussion in Section 4.1). The rate coefficients are better known, constrained, and tabulated than the cross-sections needed in the first approach. By only considering kinetic rates from https://umistdatabase.net/ (T. J. Millar et al. 2024, see Appendix B), a couple of assumptions are made:

(i) Ion-neutral collisions are treated as if they were occurring at thermal energy (with relative energy $\lesssim 10$ eV).

(ii) It indirectly means that the considered collisions change the reactants (reactants≠products, elastic and symmetric charge-exchange collisions are not considered) as we primarily focus on the ion composition and ion-neutral chemistry. For example, symmetric charge exchange such as $O_2^+ + O_2 \longrightarrow O_2 + O_2^+$ is ignored. However, G. Carnielli et al. (2020a) showed that such a process does not affect the total number density in their simulations for the G02 flyby, keeping in mind that their ionosphere was dominated by O_2^+.

(iii) Only spontaneous reactions in the gas phase – that is, exothermic and athermic reactions (e.g. $O_2 + H_3^+ \leftrightarrow O_2H^+ + H_2$) – are considered.

(iv) Reactants and products are assumed to be in the ground state. A non-exhaustive list of reactions is missing as they involve excited states. For instance, the reaction $H^+ + H_2(\nu) \rightarrow H + H_2^+$ that is exothermic only when H_2 is in an excited vibrational state $\nu \geq 4$ (D. L. Huestis 2008) is ignored. Similarly, ions may also be left in an excited state following electron-impact ionization that is the main source of ionization within Ganymede's ionosphere, and become more reactive (e.g. $O_2^{+*} + H_2O \rightarrow O_2 + H_2O^+$, B. R. Turner & J. A. Rutherford 1968), being ignored here as well.

We fix the neutral temperature to $T_n = 100$ K. First, it corresponds to the mean temperature at Ganymede's surface (varying between 80 and 150 K, see F. Leblanc et al. 2017). Secondly, the lower it is, the higher the rate coefficient is. The simulations will overestimate ions born from chemistry if Ganymede is warmer (putting aside that we have used rate coefficients and not cross-sections as discussed in Section 4.1). As a first application to Ganymede, the main goal is to provide a qualitative understanding of how ion-neutral chemistry may affect the exo-ionosphere of icy moons in the magnetized case.

At each time-step, we draw a random number p following a uniform distribution on the interval [0,1] (i.e. $p \in \mathcal{U}_{[0,1]}$) and compare to $p_{\rm collision}$. If $p < p_{\rm collision}$, there is collision, none otherwise. The collisionless version of the test particle is equivalent to $p_{\rm collision} = 0$. In case of a collision, we need to identify the neutral species with which the ion species i has collided. We estimate the probability $p_{i,n}$ for the ion species i to collide with the neutral species n given by

$$p_{i,n} = \frac{\nu_{i,n}}{\sum_j^{\rm neutrals}\nu_{i,j}} \quad (8)$$

such that $\sum_n^{\rm neutrals} p_{i,n} = 1$.

Note that for accuracy, Δt must obey $\nu_{i,n}\Delta t \lesssim 1$: A maximum of only one collision must occur during Δt or, more precisely, the probability to have 2 or more collisions during a time-step must remain low. That approximation holds at Ganymede. A quick way to estimate the maximum ion-neutral collision frequency is to multiply the maximum neutral number density, found in general at the surface, with the largest kinetic rate coefficient to get an upper limit for $\nu_{i,n} = k_{i,n}n_n$. The maximum neutral number density is $\sim 3\times10^{15}$ m^{-3} (cf. Appendix A in A. Beth et al. 2025) and the maximum rate coefficient is around $\sim 10^{-14}$ m^3 s^{-1} (typical order of magnitude at $T_n = 100$ K for reactions with water) such that the ion-neutral collision frequency is $\lesssim 30$ s^{-1}. Δt is mass-dependent and varies from 1.7×10^{-3} s for H^+ to 5.5×10^{-2} s for O_2H^+. $\nu_{i,n}\Delta t$ is found to be maximal by far for any ion colliding with H_2O, up to ~ 0.53 at the surface for $O^+ + H_2O$ and therefore still below 1. As the occurrence of collisions follows a Poisson distribution if collisions are independent (though not completely true as the order of the collisions matters and these collisions change the nature of the ions), the probability for no collision, in that case, is $\exp(-0.53) \approx 58.8$ per cent, only 1 collision 31.2 per cent, and 2 or more 10 per cent that we found acceptable to not constrain against chemistry. In a less magnetized environment, Δt would have to be adapted with respect to $\nu_{i,n}$ instead. Our approach is valid in the limit $\nu_{i,n} \lesssim \omega_{c,i}$, hence perfect for Ganymede where the ion motion is dominated by electromagnetic fields and not collisions owing to Ganymede's own magnetic field. As the ion moves farther away from the moon, the ion-neutral collision frequency decreases with the decrease in the neutral number density. Therefore, $\nu_{i,n}\Delta t$ decreases with altitude as Δt is fixed for a given ion. Including collisions increases the computational time compared to the collisionless case: Drawing random numbers requires more time (roughly + 50-100 per cent). To keep the simulation time reasonable, we have reduced the number of simulated macroparticles generated tenfold (that said $N_{\rm stat} = 10^3$ instead of 10^4 in A. Beth et al. 2025). This increases the numerical noise (roughly 3 times larger than those from A. Beth et al. 2025, as the standard deviation scales with $1/\sqrt{N_{\rm stat}}$) in the number density profiles. The most affected ion species are Jovian H^+ and O^+ and those with a low statistic, hence number density.

Along with the ion-neutral chemistry and the formation of new ion species, we have also considered the excess energy following the collision. As reactions considered here are exothermic (eventually athermic), the excess energy must be dissipated somehow. In the present model, we assume that the excess energy is only converted

Downloaded from https://academic.oup.com/mnras/article/544/1/95/8269935 by Imperial College of Science Technology and Medicine user on 06 November 2025

Table 1. Configuration of the different flybys considered for our simulations. Adapted from A. Beth et al. (2025).

Flyby	Location							$< \vec{v}_{SC} >$		
	Rel. to the PS	∠ Sun-Jup.-Gan.	Rel. to Ganymede	Plasma regions	$r\ [R_G]$	CA lat.	long.	$< v_{SC,x} >$	$< v_{SC,y} >$ (km s^{-1})	$< v_{SC,z} >$
G01	↑	349°	central wake		1.32	30.6°	−21.1°	2.08	7.30	1.12
G07	↓	115.5°	mid-lat. downstr.	Alfvén wing	2.18	55.6°	2.9°	0.46	−8.43	−0.04
G29	↑	178.5°	mid-lat. downstr.		1.89	62.4°	1.4°	−0.12	10.45	−0.07

into kinetic energy and redistributed between the products. This is described in detail in Appendix C.

3 RESULTS

In this section, we present the results of our simulations, which include ion-neutral chemistry, for three different Galileo flybys: G01, G07, and G29. We choose these flybys for several reasons. They were all performed in the Alfvén wings, when Ganymede was outside the plasma sheet, and showed the best model-data agreement (A. Beth et al. 2025). Furthermore, these flybys are associated with different Ganymede's local time. For G01, the Sun illuminated the anti-Jovian side of Ganymede. In contrast, for G07, the trailing hemisphere, slightly towards the Jovian side, was illuminated. G29 flyby was performed when Ganymede passed through Jupiter's shadow, which corresponds to an H_2O-deficient exosphere, mainly produced by sputtering and radiolysis, with photoionization turned off. We summarize the characteristics of these flybys in Table 1. First, we have performed simulations along the flybys' trajectories to be compared with results from A. Beth et al. (2025) (see Section 3.1). Next, we have performed 3D cuts of ion number densities for the configurations met during these flybys (see Section 3.2). All the results are discussed and shown in the GPhiO coordinate system, centred on Ganymede, where X points in the direction of the incident plasma flow, Y points towards Jupiter, and Z completes the orthogonal system.

3.1 Along the trajectory of Galileo's flybys: G01, G07, and G29

Fig. 1 shows the ion number densities (left) and composition (right) for G01, G07, and G29. These results should be compared with Fig. 5 from A. Beth et al. (2025) without collisions. In addition to H^+, H_2^+, O^+, HO^+, H_2O^+, and O_2^+, three new ion species are included in the new simulations as these species only stem from ion-neutral collisions: H_3^+, H_3O^+, and O_2H^+ (see Appendix B).

First, ion-neutral chemistry does not modify the total ion number density. The main reason is that ions are primarily all drifting at the same velocity regardless of their mass within Ganymede's ionosphere (A. Beth et al. 2025). Ionospheric ions drift at the same perpendicular velocity perpendicular to $\vec{B}$ (i.e. $\vec{E} \times \vec{B}/B^2$ where $\vec{E}$ and $\vec{B}$ are the electric and magnetic fields from the MHD simulation) as the simulations assume ideal MHD (X. Jia et al. 2008, 2009). Ion parallel velocities (negligible at the surface) increase as ions move away from Ganymede's surface and get closer to the magnetopause: The parallel velocity is mass-dependent, hence attributed to finite Larmor radius effects (A. Beth et al. 2025). Therefore, the total ion number density is expected to change only where ion velocities depart from each other; that said, around the magnetopause or the edges of the Alfvén wings, due to ion-neutral chemistry. We do not observe such a change in our simulations as the mean mass (white solid line) at the magnetopause (MP) is barely changed compared with the collisionless case (Fig. 1, right column). Indeed, the Jovian plasma density is not yet depleted at the MP, O_2^+ number density is the same as for the collisionless case, and ionospheric ions (H_2O^+, HO^+, O^+, and a fraction of H_2^+), as they react, are mainly turned into H_3O^+ that has a mass close to the mean one in the collisionless case (going from 10 to 20 u, with an average of 14 u for the Jovian plasma). The main deviation of the mean ion mass between the collisionless case and the collision case is observed before the G01 closest approach. Dominated by H_2^+ and O_2^+ in the collisionless case, it is now dominated by O_2^+ and water-group ions: Part of H_2^+ has been converted either directly to H_2O^+/H_3O^+ or indirectly through the intermediate formation of H_3^+.

For all flybys, before inbound and after outbound MP crossings, the Jovian ion number density is unperturbed by ion-neutral collisions. Although our neutral exosphere extends up to 5 R_G, the neutral number density remains low ($\lesssim 10^{11}$ m^{-3}, A. Beth et al. 2025); hence, the collision probability mainly driven by H_2 at these altitudes is four orders of magnitude lower compared with that at the surface.

For G01 within Ganymede's magnetosphere, the O_2^+ number density does not change either, as this ion species does not react with any neutral species included in the model: It is a terminal ion. In our simulation, it can only be lost through transport, as dissociative recombination is ignored as it is negligible. Indeed, compared with ion-neutral collision frequency, for dissociative recombination to be of the same order of magnitude would require a plasma number density to be 10^7 cm^{-3} at least, whereas a posteriori it is less than 10^5 cm^{-3} from the simulations. Although a few ion-neutral reactions, namely charge exchange, lead to O_2^+ production, they remain far less efficient than the direct ionization of O_2. The production of O_2^+, through charge exchange or ionization, relies on O_2. This neutral species is confined near the surface with the lowest scale height amongst neutral species, around 20 km. Although produced only near the surface, O_2^+ is efficiently transported from the surface on the trailing side, through the whole ionosphere (cf. streamlines in O_2^+ panel) and contributes mostly to the ion composition. In addition, H_3^+ and H_3O^+ contribute significantly to the ion composition (see Fig. 1, top panel). The main chemical pathways for producing these ions are as follows:

$$H_2^+ + H_2 \longrightarrow H_3^+ + H, \tag{9}$$

$$H_3^+ + H_2O \longrightarrow H_3O^+ + H_2, \tag{10}$$

$$H_2O^+ + H_2O \longrightarrow H_3O^+ + HO. \tag{11}$$

Interestingly, H_2O^+ number density is equal to or even slightly higher than in the collisionless case. This suggests that the primary path for forming H_3O^+ is not through the loss of H_2O^+ but through that of H_3^+, and that an ion-neutral reaction leads to the production of H_2O^+. Given the neutral composition (mainly O_2, H_2, and H_2O), number densities, and by looking at the initial 'identity' of the macroparticle at the start of the simulation, we determined that H_2O^+ is also produced through charge exchange:

$$H_2^+ + H_2O \longrightarrow H_2O^+ + H_2. \tag{12}$$

Downloaded from https://academic.oup.com/mnras/article/544/1/95/8269935 by Imperial College of Science Technology and Medicine user on 06 November 2025

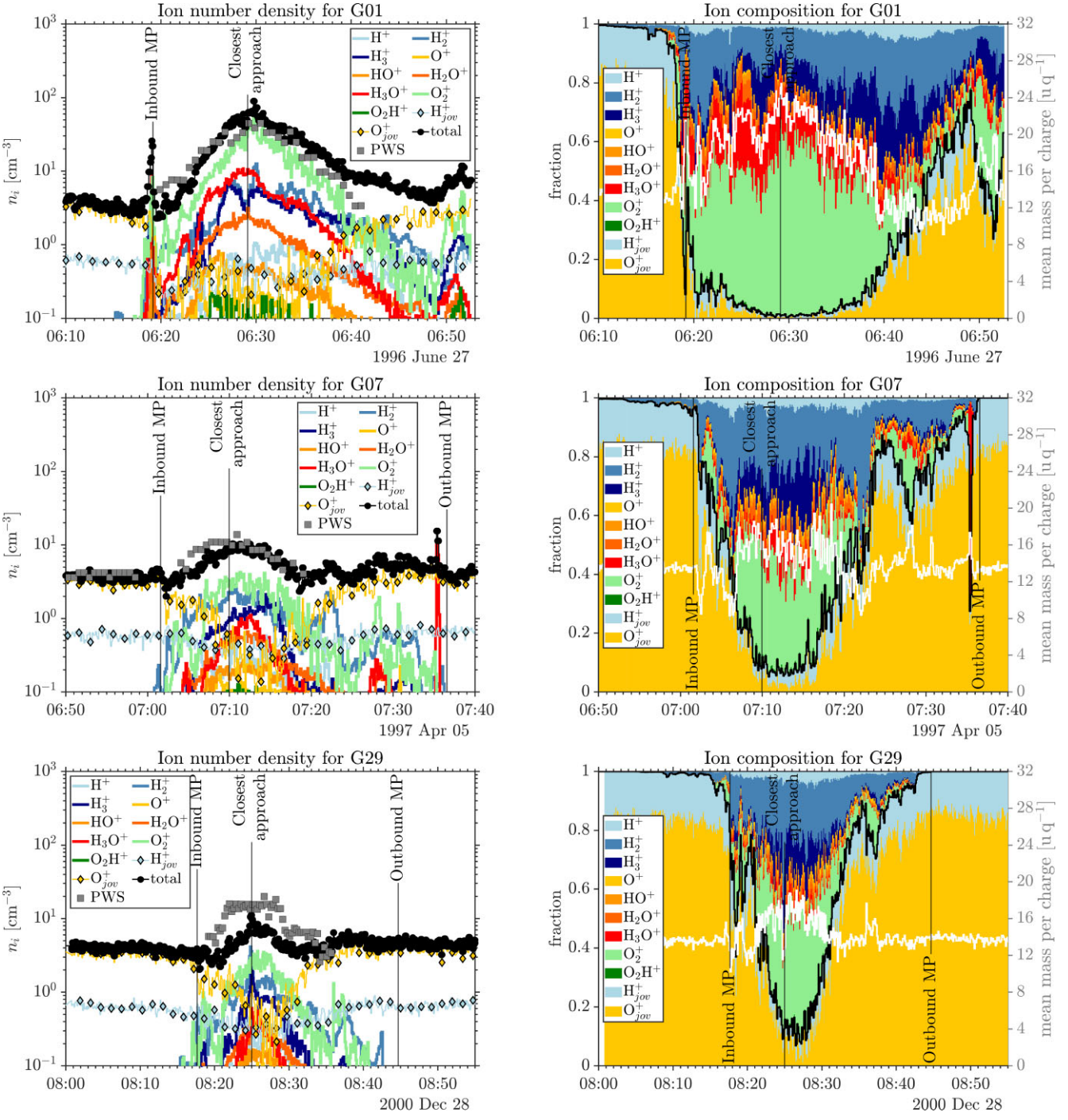


Figure 1. Simulated ion number densities for Jovian and ionospheric ions compared with in situ PWS electron number density from J. Ansher et al. (2017) (left column) and simulated ion composition (right column) during G01 (top row), G07 (middle row), and G29 (bottom row) flybys. Vertical, black lines feature the inbound magnetopause crossing, the closest approach, and the outbound magnetopause crossing (if available from the MAG data), respectively. For the ion composition, the black, thick line represents the fraction of Jovian ions. The white, thick line must be read with the right axis and corresponds to the mean ion mass per charge.

Therefore, H_2^+ number density decreases to the benefit of H_3^+ and H_2O^+ formation.

As H_2 is relatively uniform around Ganymede (i.e. with a roughly spherical symmetry), H_2^+ production and H_2^+ loss/H_3^+ production are also expected to be uniform around the moon. Unlike H_2, H_2O is primarily produced from the sublimation of the water ice on the surface: It is mainly present on the sunlit side. Galileo crossed the terminator plane from the sunlit side to the dark one around 06:33 (cf. fig. 12 in A. Beth et al. 2025), H_3^+ reacts with H_2O to become H_3O^+. As illustrated in Fig. 1 (top row), beside O_2^+ which dominates around CA, H_3^+ is more present on the dark side owing to the lack of H_2O whereas H_3O^+ is mainly formed on the sunlit side.

For G07 and G29 (cf. Fig. 1, middle and bottom rows), the change in ion composition is even less dramatic as these flybys were performed much farther away from Ganymede (resp. 2.18 and 1.89 R_G to compare with 1.32 R_G for G01 at closest approach). For

Downloaded from https://academic.oup.com/mnras/article/544/1/95/8269935 by Imperial College of Science Technology and Medicine user on 06 November 2025

G07, H_2^+ number density is mainly reduced between 07:05 and 07:15 compared with the profiles from A. Beth et al. (2025) as it is turned into H_3^+ (directly through proton transfer with H_2), H_2O^+ (through charge exchange with H_2O), and H_3O^+ (either directly through proton transfer with H_2O, or indirectly through two successive proton transfers, first with H_2 and then H_2O). We observed an asymmetry in the H_3^+ ion number density. While most ion number densities peak at closest approach, H_3^+ number density peaks slightly later around 07:12-07:15, interestingly corresponding to local midnight in terms of 'illumination' in Ganymede's frame (cf. fig. 12 in A. Beth et al. 2025). In addition, right before the G07 outbound MP crossing, the plasma peak is dominated by H_3O^+ instead of H_2O^+ in the collisionless case (to be compared with fig. 5 in A. Beth et al. 2025). Although the outbound MP crossing occurs on the dark side (cf. fig. 12 from A. Beth et al. 2025) where H_2O number density is much lower, hence water-group ions are less likely to be produced, G07 was the only flyby going from the sub-Jovian to the anti-Jovian flank (i.e. away from Jupiter), and therefore in the direction/hemisphere where ionospheric ions are picked up, along the convective electric field $\vec{E}_{\text{conv.}} = -\vec{v}_{\text{jov}} \times \vec{B}$ that points towards $-y$ ($\vec{B}$ mainly points towards $-z$ and the Jovian plasma velocity $\vec{v}_{\text{jov}}$ points towards $+x$ such that $\vec{E}_{\text{conv.}}$ points towards $-y$). Therefore, the presence of H_3O^+ is consistent with the fact that H_2O^+ (from which H_3O^+ originates here) is produced on the dayside (Galileo crossed the terminator plane before the inbound MP crossing, cf. fig. 12 from A. Beth et al. 2025), then transported upstream (i.e. in the $-x$ direction towards the trailing side of the magnetopause) inside Ganymede's magnetosphere, and finally deflected either along the MP preferentially along the anti-Jovian flank and along/within the Alfvén wings. That is shown in more detail in Section 3.2.

G29 is the least affected flyby by ion-neutral chemistry. As Ganymede was within Jupiter's shadow, H_2O is much lower and only produced through ice sputtering. With low H_2O number density, H_2^+ reacts either with H_2 to produce H_3^+, or with O_2 to be turned into O_2^+ or O_2H^+. On the one hand, the lack of H_2O minimizes the loss of H_2^+/H_3^+ (and O_2H^+ though negligible). On the other hand, the lack of photoionization due to eclipse drastically impedes the production of H_2^+, the precursor for forming H_3^+ and O_2H^+ (see Section 4.3). H_3^+ and O_2H^+ are less likely to be produced but also less likely to be lost. However, in the case of G29, ionization only relies on electron impact, which is poorly constrained.

For all flybys, the most affected ion species by ion-neutral chemistry is O^+. For example, for G01, the simulated ionospheric O^+ number density reaches $\sim 10\,\text{cm}^{-3}$ at closest approach in the collisionless case (A. Beth et al. 2025), whereas it only reaches $\sim 0.5 - 0.7\,\text{cm}^{-3}$ once ion-neutral collisions are considered. O^+ reacts with all the different neutral species present in Ganymede's exosphere, while it is mainly produced through ionization of H_2O and O_2. This deficiency found for O^+ has strong implications on the interpretation of previous flybys regarding ion composition (see Section 4.2).

3.2 3D spatial distribution

Figs 2–4 show different cuts (in the XY, XZ, and YZ planes in the GPhiO coordinate system centred on Ganymede) of number densities of the different ion species for the three flybys considered, G01, G07, and G29, respectively. These cuts help to reveal different asymmetries: dayside/nightside (except for G29 eclipsed by Jupiter) and Jovian/anti-Jovian.

A common feature of G01 and G07 is the absence of H_2^+ and H_3^+ (and of O_2H^+ and O^+ to a lesser extent) near the subsolar point in the few tens of kilometres above the surface (seen as a faint white crescent, in the case of a lack of macroparticles, or a black one, in the case of very low number densities, present at the edge of the disc that defines Ganymede). As H_2^+ macroparticles, which are also the sole 'parent' of H_3^+, are supposed to be produced homogeneously through the simulation box (regardless of the neutral number density that only affects their statistical weight), this low amount (black crescent) of H_2^+ means that the macroparticle is readily turned into another, but which one? A priori, near the surface, the main loss mechanisms for H_2^+ are charge exchange and proton transfer with O_2, producing O_2^+ and O_2H^+, respectively, as O_2 is much denser than H_2 at the surface. This loss of H_2^+ and production of O_2H^+ (only produced through ion-neutral chemistry, O_2^+ being mainly yielded through O_2 ionization) must occur homogeneously around Ganymede, as O_2 and H_2 do not exhibit strong spatial dependency. However, near the subsolar point, there is the extra presence of sublimated H_2O. This large amount of H_2O, larger than those of O_2 and H_2 (A. Beth et al. 2025), increases the loss of H_2^+, yielding H_2O^+ and H_3O^+. This also causes H_2O^+ to be under photo-chemical equilibrium near the subsolar point, reaching a number density of $\sim 15 - 20\,\text{cm}^{-3}$ (the crescent has the corresponding colour). As a matter of fact, H_2O reacts with all ions except O_2^+ and H_3O^+, driving their loss over the subsolar point to ultimately become H_3O^+ through successive ion-neutral reactions (see Appendix B and Section 4.3).

Still in the case of G01 and G07, we also found that ion-neutral chemistry contributes non-negligibly to H_2O^+ production rate via charge-exchange with H_2O. In the collisionless case, H_2O^+ is solely produced through ionization of H_2O.

G29 is a case of its own: Ganymede passed in Jupiter's shadow, inhibiting the presence of H_2O and photoionization. Consequently, it allows us to focus solely on the Jovian/anti-Jovian asymmetry. Overall, ion number densities are lower owing to the absence of photoionization and of sublimated water when comparing with the other flybys on the dayside. Removing H_2O from the chemical network leads to a few changes as well. H_3O^+ production is still possible but unlikely (it can be formed from O^+ and successive proton transfer with H_2), H_3^+ and O_2H^+ become terminal ions (see Section 4.3). Therefore, we anticipate that the ion composition may change during the JUICE escorting phase while passing behind Jupiter. Although O_2H^+ survives longer in these conditions, it remains confined at the surface where O_2 resides. Afar from Ganymede, O_2H^+ is turned into H_3^+ through proton transfer with H_2.

In all cases, Ganymede's plasma tail is asymmetric and more extended on the anti-Jovian side (cf. XY cut, left and centre panels for each species), populated by heavy ions. As ionospheric ions escape Ganymede's magnetosphere upstream (cf. the streamlines), they are picked up in the direction of the convective electric field. Ions are transported, surfing along the magnetopause before leaving the system downstream, forming a tail in front of the moon. When the subsolar point, where the water ice sublimates the most, is located on the far side of Jupiter, as for G01, the plasma is loaded with water ions (H_2O^+ and H_3O^+). It is unclear if 'mass-loading' would be the most appropriate term here as the Jovian plasma has a mean mass-to-charge ratio of $m/z = 14\,\text{u}\,\text{q}^{-1}$ while water ions do not have a mass drastically different. However, it may affect the plasma dynamics as these ions are injected at a much lower speed than the ambient plasma flow: It would be then 'momentum-(un)loading'. For instance, for G01, in Fig. 2, for O_2^+, H_2O^+, and H_3O^+, we can identify the cycloidal

Downloaded from https://academic.oup.com/mnras/article/544/1/95/8269935 by Imperial College of Science Technology and Medicine user on 06 November 2025

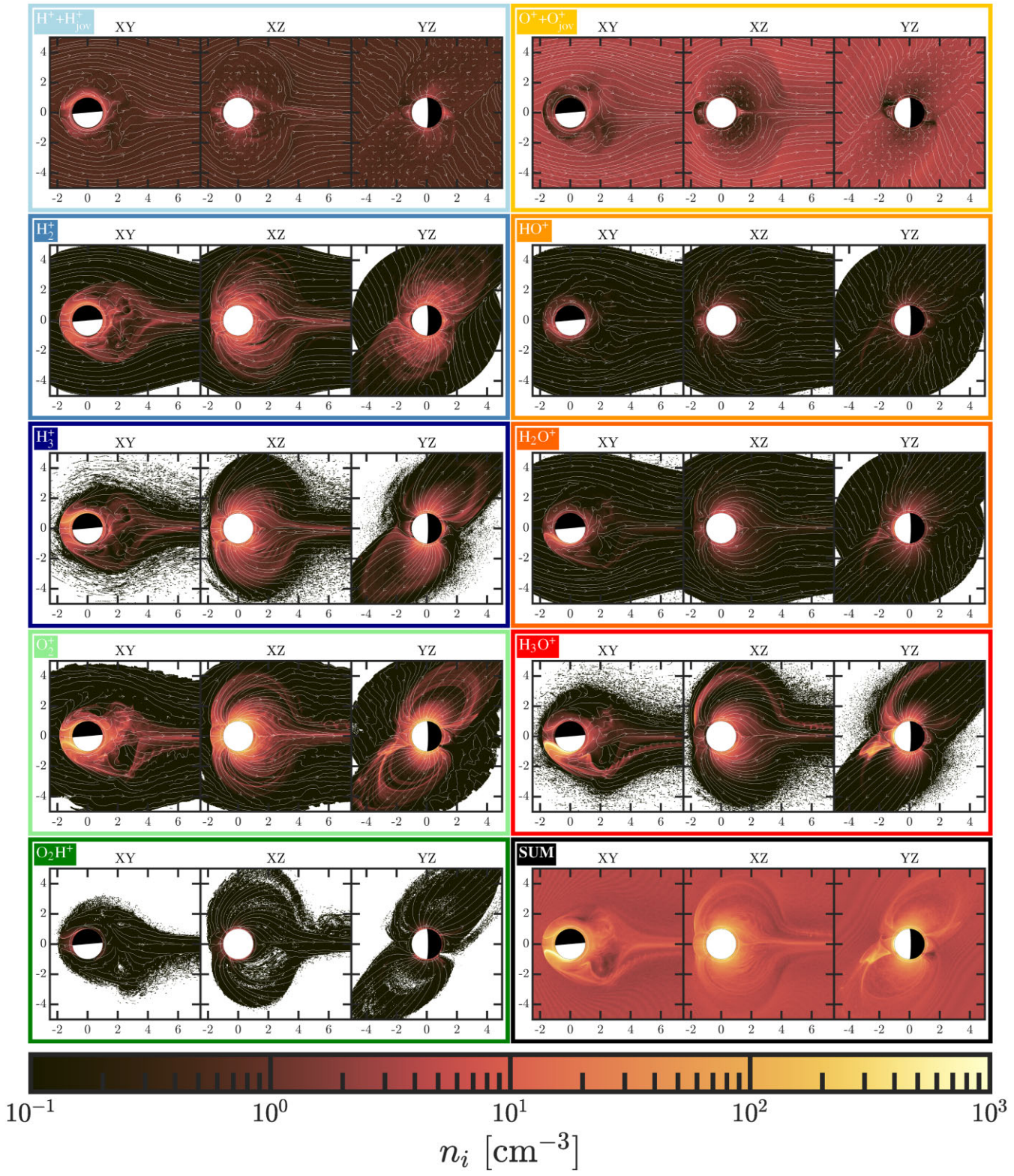


Figure 2. Cuts of ion number densities in the different planes around Ganymede for G01. The cuts are made in the XY, YZ, and YZ planes in the GPhiO coordinate system. The axes' unit is in Ganymede's radius. The three upper left panels correspond to light ions: H^+ (both jovian and ionospheric), H_2^+, and H_3^+. The four upper right panels correspond to intermediate-mass (or water-group) ions: O^+ (both jovian and ionospheric), HO^+, H_2O^+, and H_3O^+. The two bottom left panels correspond to heavy ions: O_2^+ and O_2H^+, H_2^+. The bottom right panel corresponds to the total ion number density. Ion species are indicated in the top left corner of each frame. The central disk corresponds to Ganymede. The white part of the disk is the dayside. Any white area outside Ganymede corresponds to regions that macroparticles have not reached or because their weight was 0 (they are launched from a cell where the neutral number density is 0). The thin white circle around Ganymede is located at 500 km which corresponds to one of the two radii of JUICE circular orbits. We plotted the streamlines for each ion species, with arrows indicating the flow direction.

Downloaded from https://academic.oup.com/mnras/article/544/1/95/8269935 by Imperial College of Science Technology and Medicine user on 06 November 2025

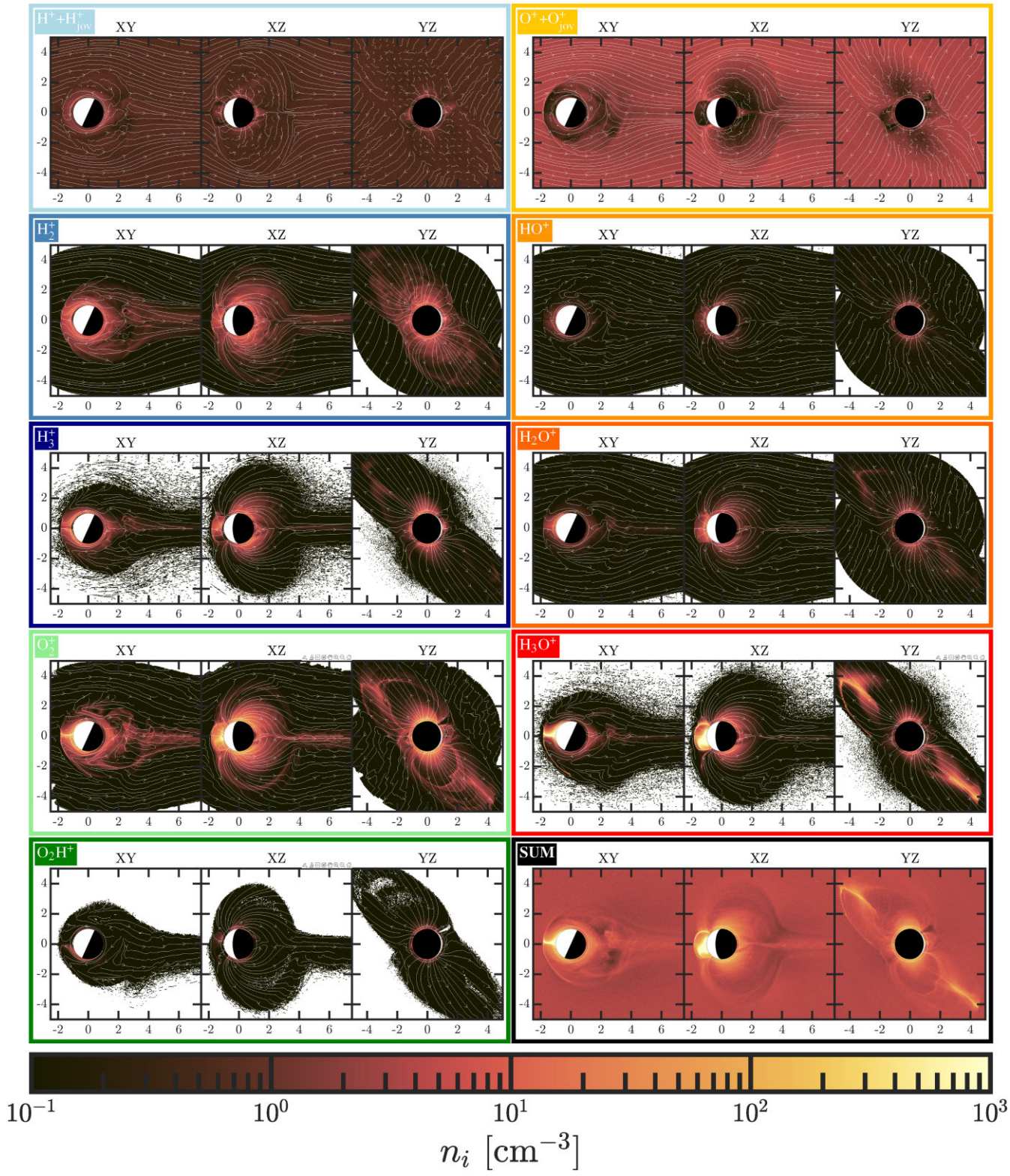


Figure 3. Similar to Fig. 2 for G07.

motion of these heavy ions downstream along the wake. If one wants to include ionospheric ions in the simulation (in particular heavy ions with a large gyroradius), one must consider simulating them kinetically with a hybrid approach. This partly explains why MHD simulations might struggle to accurately capture the magnetopause crossings, in particular along the anti-Jovian flank of Ganymede's magnetosphere, in the wake, and on the dayside (e.g. S. Duling et al. 2022), as the plasma may be momentum-loaded by ionospheric heavy ions with large gyroradii effects.

Another way to summarize our findings is to look at the dominant ion species around Ganymede. Fig. 5 shows cuts of the dominant ion species for the different flybys. Therein, we define regions around

Downloaded from https://academic.oup.com/mnras/article/544/1/95/8269935 by Imperial College of Science Technology and Medicine user on 06 November 2025

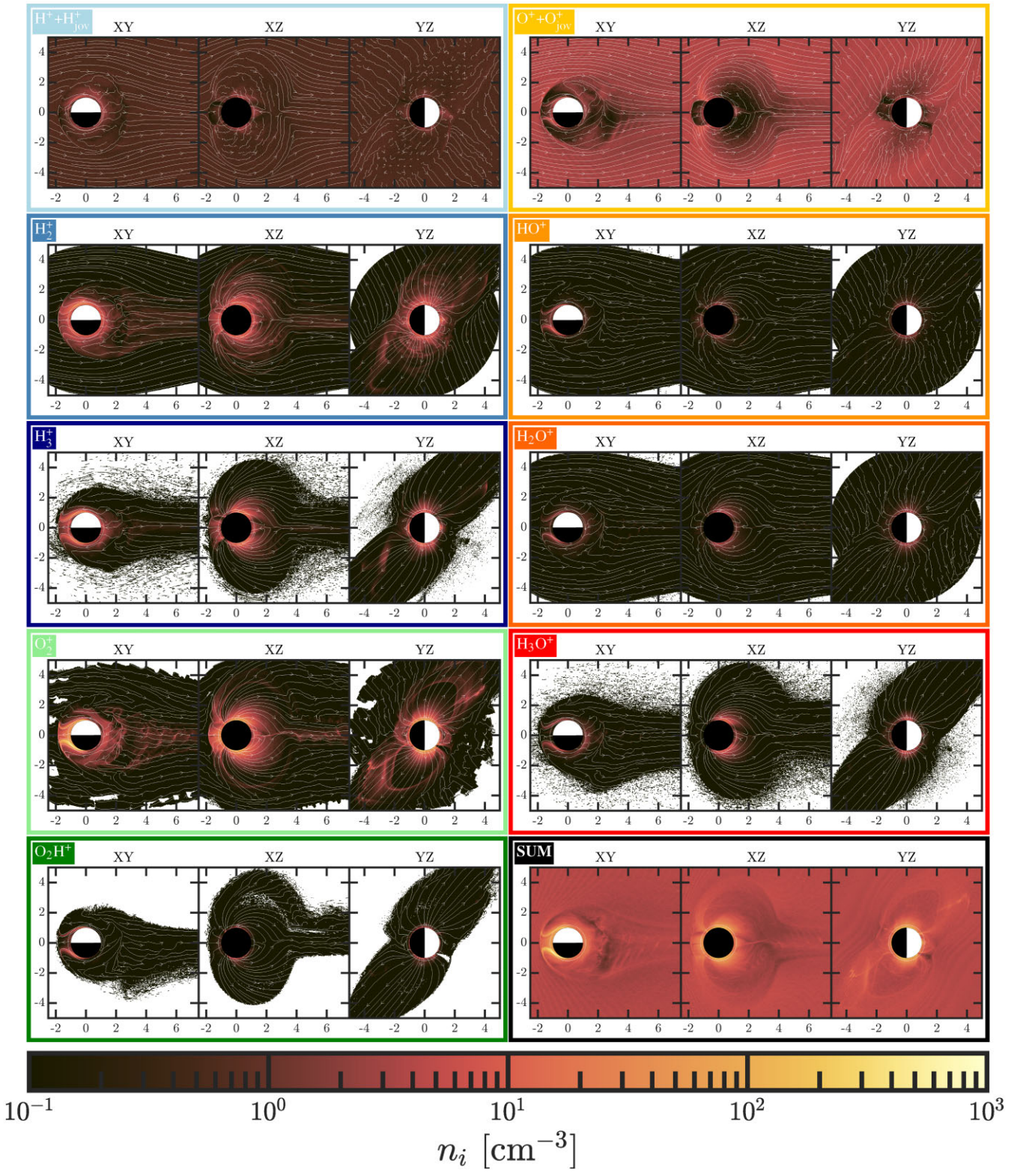


Figure 4. Similar to Fig. 2 for G29. Ganymede was in Jupiter's shadow, though we still indicate the expected dayside.

Ganymede depending on the ion species with the largest number density for the three analysed configurations, G01 (top row), G07 (middle row), and G29 (bottom row). This reveals the extent of Ganymede's ionosphere. Although the ionosphere does not have a strict upper boundary, it is appropriate to say that it extends as far as the plasma of exospheric origin dominates over that of magnetospheric origin. For O^+ and H^+, we considered together ions of both ionospheric and magnetospheric origins. Outside of Ganymede's magnetosphere, Jovian O^+ dominates the plasma composition. Even though the Jovian magnetospheric plasma may still access part of Ganymede's magnetosphere, even the closed-field-line region (extending roughly up to $\sim 2R_G$ from the centre of Ganymede in its equatorial plane)

Downloaded from https://academic.oup.com/mnras/article/544/1/95/8269935 by Imperial College of Science Technology and Medicine user on 06 November 2025

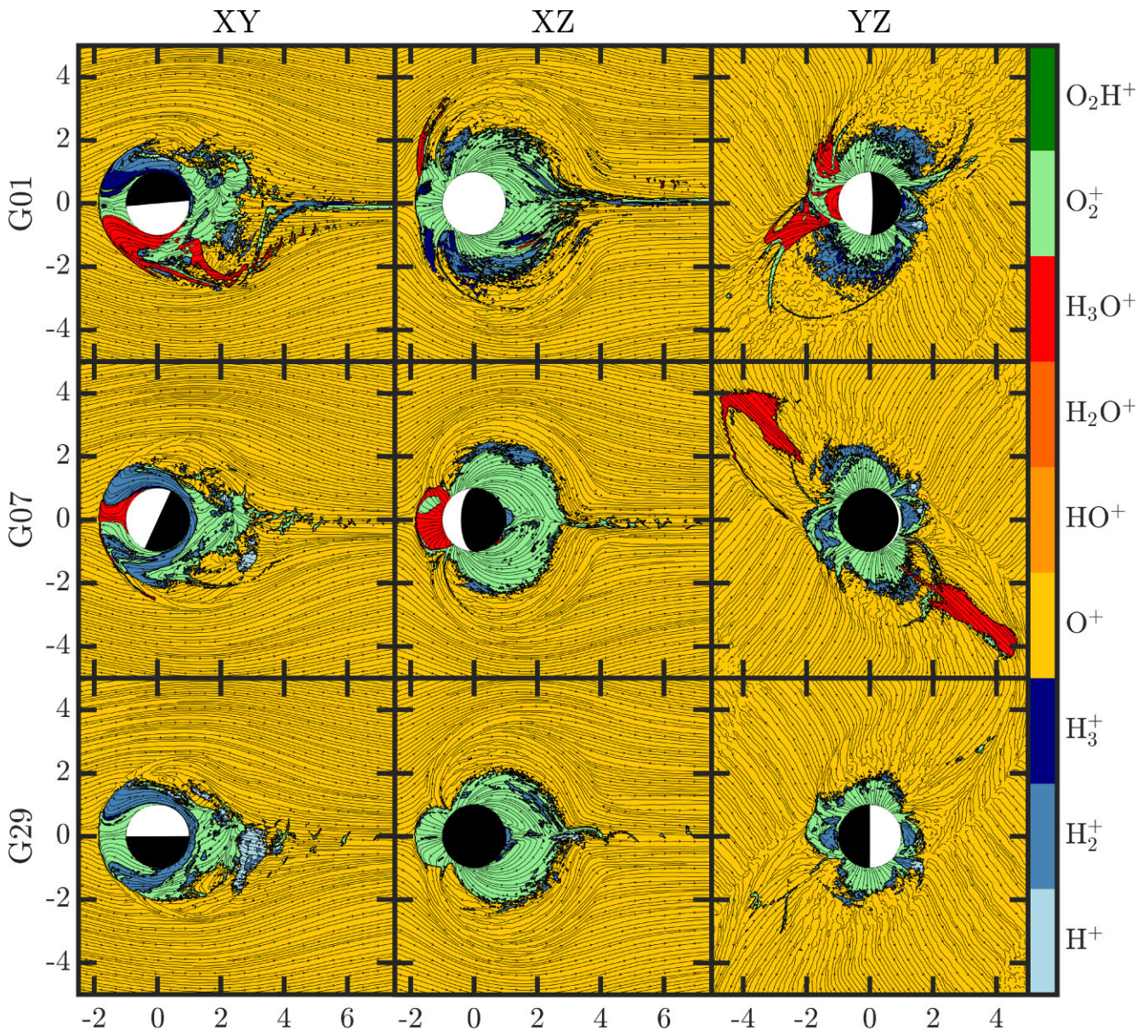


Figure 5. Cuts for G01, G07, and G29, as Figs 2–4, coloured as a function of the dominant ion species. Note that Ganymede is within Jupiter's shadow for G29. Where O^+ and H^+ dominate, this is solely caused by Jovian contribution. Streamlines of the total ion momentum are superimposed.

via the wake, the ionospheric plasma dominates within $\sim 1 R_G$ from the surface. During G29, Ganymede's ionosphere shrinks in size compared to other flybys due to the absence of sublimation and photoionization.

Fig. 5 emphasizes the importance of the location of the subsolar point compared to the overall magnetospheric configuration of Ganymede (i.e. depending on Ganymede's position relative to Jupiter's dipole). Depending on the location of the subsolar point (e.g. G01 versus G07), H_3O^+ may be the dominant ion species around the subsolar point within Ganymede's magnetosphere. H_3^+ is expected to be more present on the dark side (cf. G01). However, in the case of G07, the dark side and leading hemispheres coincide. The plasma within Ganymede's magnetosphere flows in the -x direction around the moon, sputtering the leading hemisphere (G. Carnielli et al. 2020b). H_3^+ is therefore convected towards the shadowed surface, where it reacts with O_2: A thin layer of O_2H^+ is seen in Fig. 3 on the nightside.

Our simulations agree with the findings of A. Eviatar et al. (2001) on the fact that O_2^+ dominates the composition over the polar regions (cf. XZ and YZ cuts). However, while A. Eviatar et al. (2001) concluded that O^+ dominates at low latitudes and flows along the open flux tubes, we found that H_3O^+ appears to be a better candidate at low latitudes.

4 DISCUSSION

In this section, we discuss a few aspects regarding our modelling, its reliability, the assumptions made, and the new questions raised by this study that must be addressed in the future.

4.1 Coefficient rates versus cross-sections

In this paper, we treat collisions using kinetic rates instead of cross-sections in part due to a lack of laboratory measurements (see

Downloaded from https://academic.oup.com/mnras/article/544/1/95/8269935 by Imperial College of Science Technology and Medicine user on 06 November 2025

Section 2.2). Considering kinetic coefficient rates instead of cross-sections might overestimate the effect of ion-neutral chemistry, but this might not be drastically the case in our case study. Let's take the example of $H_2^+ + H_2$ presented in fig. 4 of A. V. Phelps (1990). Below a laboratory ion energy $E_{\rm lab.}$ of 5 eV ($E_{\rm rel.} < 2.5$ eV, cf. Appendix C), the formation of H_3^+ dominates the process, and the ion-neutral collision can be well approximated by the Langevin model (see e.g. J. L. Fox 2015, which describes the interaction between an ion and a non-polar molecule), meaning that using a coefficient rate is appropriate (i.e. $<\sigma v_{\rm rel.}>_{H_2^+-H_2}(E_{\rm lab.} < 5\,{\rm eV}) \sim$ const. $\approx 2.08 \times 10^{-15}\,{\rm m^3\,s^{-1}}$). Above 5 eV, symmetric charge exchange dominates the interaction by forming a slow H_2^+ and a fast H_2. Because the cross-section becomes roughly constant at these energies ($\sigma_{H_2^+-H_2}(E_{\rm rel.} > 5\ {\rm eV}) \sim 10^{-19}$ ${\rm m^{-2}}$), $<\sigma v_{\rm rel.}>$ must be calculated using equation (6) instead and hence it increases with energy, linearly with respect to the relative speed (as the relative speed is well above the thermal neutral speed): $<\sigma v_{\rm rel.}>_{H_2^+-H_2} \sim 10^{-19}\|\vec{v}_{\rm rel.}\|\,{\rm m^3\,s^{-1}}$ (quantities given in SI units). As shown in A. Beth et al. (2025) and Fig. E1, within Ganymede's magnetosphere, light ion species remain below $\sim$ 20 eV, this limit being reached around the MP. Nevertheless, at the MP, H_2 number density has already decreased by two orders of magnitude compared with that at the surface. Therefore, it would require H_2^+ to be around 40 keV at the MP (i.e. 10 times faster than the Jovian magnetospheric flow) to have the same collision probability than that at the surface. Even if we virtually underestimate cross-sections at large energies, the likelihood of ion-neutral collisions at these energies is still negligible owing to drastically lower neutral number densities. Most of the ion-neutral chemistry occurs near the surface where neutral number densities are large and ions are slow (that said $E_{\rm ref.} < 5$ eV). Therefore, we anticipate that the use of the reaction rate coefficient remains valid with the electromagnetic fields used in these simulations.

As pointed out by A. Beth et al. (2025), using the electromagnetic fields from X. Jia et al. (2008, 2009), there are still discrepancies between simulated and observed ion energies (observed ion energies exceed those simulated, see fig. 7 in A. Beth et al. 2025, and Appendix E1), suggesting that ions, in particular heavy ones, such as water ions and O_2^+, may exceed this threshold of 5 eV even near the surface of Ganymede. Processes at higher energies (i.e. not thermal and/or endothermic such as charge-exchange, dissociation, and excitation), above tens of eVs, are not considered here as they tend to be endothermic and require cross-sections. The ion species most likely to exceed these threshold energies are the heaviest because all species tend to drift at similar speeds with these ideal MHD background fields (A. Beth et al. 2025) such that their kinetic energy is only a function of their mass. For example, let's look at reactions that involve heavy ions, such as $O_2^+ + H_2$: O_2^+ is heavy and H_2 has the most extended exosphere with the largest scale height. These species do not react together at thermal energy in the ground state (hence not included in our chemical network) but do at much larger energies (A. Irvine & C. Latimer 1997). In addition, one has also to consider the energy states of the reactants. For example, the excited metastable O_2^+ is more reactive than O_2^+ in the ground state (namely $X_2\Pi_g$): The former has a charge-exchange cross-section with $H_2 \sim 30$ times larger at 100 eV than the latter (A. Irvine & C. Latimer 1997). Likewise, O_2^+ may be left in an excited state following electron impact (B. R. Turner & J. A. Rutherford 1968), the primary ionization source at Ganymede (G. Carnielli et al. 2019). Therefore, not only the state in which ions are born, ground or excited, depending on the ionization process (photon or electron impact), but also the electromagnetic fields, may affect the ion-neutral chemistry and the outcome of our simulations. This must not be forgotten. On the one hand, little is known about the formation of excited states and branching ratios (see also Section 4.3). On the other hand, we still miss proper constraints of the 3D electromagnetic fields (the electric field being unknown) around Ganymede.

4.2 Insight on Juno PJ34 flyby

Although the current work does not focus on the Juno flyby (that is left for future studies), our modelling includes the production of H_3^+ that was detected during the PJ34 Juno flyby. Therefore, our simulations can help us interpret the findings of P. W. Valek et al. (2022). One finding was the inbound-outbound asymmetry in the H_3^+ number density. During PJ34, inbound occurred on the nightside, whereas outbound occurred on the dayside. Consequently, Ganymede's exosphere is expected to be denser and wetter (more H_2O) along the outbound leg. That may explain the H_3^+ asymmetry (i.e. a steeper decrease of the number density as a function of the altitude): H_3^+ is lost and turned into H_3O^+ as it reacts with H_2O on the sunlit side as the spacecraft approached the subsolar point.

A second finding was the 'O^+' asymmetry. It would be more appropriate to refer to it as water-group ion asymmetry as the instrument lacks mass precision. The number density of water-group ions is higher on the dayside. This might support our finding that H_2O^+ and H_3O^+ are significantly produced on the dayside where H_2O is present, misidentifying these ions as O^+.

As shown in Section 3.1, O^+ number density (both Jovian and ionospheric) is strongly depleted near Ganymede compared with the collisionless case (cf. A. Beth et al. 2025). It has been reported in the literature that O^+ was the dominant ion within Ganymede's ionosphere during Galileo's flybys (V. M. Vasyliūnas & A. Eviatar 2000) and the main contributor to the range 16–19 u q^{-1} (i.e. water-group ions) during Juno flyby (F. Allegrini et al. 2022; P. W. Valek et al. 2022). However, the ion identification from observations remains inconclusive owing to the inability to separate ion masses (e.g. Galileo) or due to a mass resolution that is too low to separate water-group ions (e.g. Juno). By including ion-neutral chemistry, we find that O^+ number density is significantly reduced: O^+ reacts with all neutral species, mainly through charge exchange (see Appendices B, D, and Fig. 6). Aside from the ionization of neutrals, it can only be produced through collision between H^+ and O (almost reversible as H and O have close ionization energy, see Appendix D), which is a negligible chemical path due to the low level of hydrogen. O^+ is destroyed and barely replenished through ion-neutral collisions compared with the collisionless case. Therefore, it is unlikely within Ganymede's magnetosphere that ionospheric O^+ is the dominant species amongst the water-group ions at low energy, especially on the dayside due to the additional presence of H_2O.

Within the context of the Juno flyby, J. H. Waite Jr et al. (2024) attempted to simulate and retrieve H_2^+, H_3^+, and O_2^+ under severe assumptions. The electron number density obtained from D. R. Buccino et al. (2022) is prescribed for the estimation of H_2^+ and H_3^+ number densities (i.e. not self-consistently calculated). Ions are assumed to be in photochemical equilibrium, neglecting transport. Applying these assumptions, including dissociative recombination, to G01 conditions for O_2^+ over the polar caps, which dominates the ion composition in this region, we infer a number density of $\sim 8 \times 10^3\,{\rm cm^{-3}}$. In contrast, in our simulations, O_2^+ ion number density reaches $\sim 1 \times 10^3\,{\rm cm^{-3}}$. This demonstrates that our model, which includes transport, is best suited for interpreting Juno observations.

Downloaded from https://academic.oup.com/mnras/article/544/1/95/8269935 by Imperial College of Science Technology and Medicine user on 06 November 2025

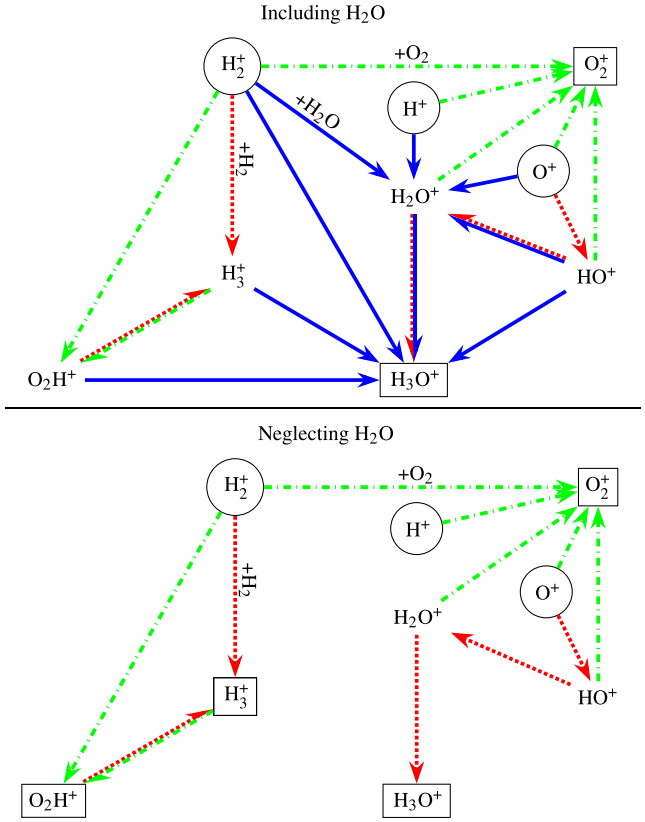


Figure 6. Chemical pathway for ion-neutral collision at Ganymede considering O_2, H_2, with (top) or without (bottom) H_2O as the main neutral species. Arrows' styles and/or colour indicate the neutral species with which ions react: dotted red for H_2, solid blue for H_2O, and dash–dotted green for O_2. Circles identify species only produced through ionization and lost through at least one ion-neutral reaction. Squares identify species that cannot be lost through ion-neutral collisions (excluding processes that are endothermic or involve excited states). Loss through ion-electron dissociative recombination is disregarded here.

4.3 Comprehensive chemical network at Ganymede

A summary of chemical pathways is shown in Fig. 6, where two cases are addressed: one with H_2O, representative of dayside, and one without, representative of nightside, in Jupiter's shadow (like G29) or farther away from the subsolar point as the scale height for the sublimated H_2O is small. H_3O^+ is expected to be a terminal ion in the presence of H_2O, whereas O_2H^+ and H_3^+ are terminal ions only in its absence. In both cases, O_2^+ is always a terminal ion. While Fig. 6 exhibits similarities with V. I. Shematovich (2008), there are differences. For example, we did not include the possibility to convert O_2^+ to O_2H^+: Such a reaction was not found in either UMIST (T. J. Millar et al. 2024) or KIDA (V. Wakelam et al. 2012) databases. However, $O_2^+ + H_2$ might produce O_2H^+ and H_2O^+ if O_2^+ is an excited state (J. M. Ajello et al. 1974; M. E. Weber et al. 1993). This suggests that we might be able to infer whether O_2^+ is excited depending on the amount of O_2H^+ (and maybe H_2O^+) that Jupiter Icy Moons Explorer (JUICE) will ever detect. Times when Ganymede will be in Jupiter's shadow must be of particular interest: The ionization is driven solely by electron impact and H_2O number density is highly reduced, hindering the ability to produce H_2O^+ from H_2O through ionization. H_2O^+ will then be only produced through ion-neutral chemistry and these aforementioned chemical pathways. This again highlights the importance of considering the energy state of ions.

The recent discovery of a localized CO_2 gas patch by D. Bockelée-Morvan et al. (2024), though low in terms of number density, may affect the ion composition and our findings. First, including CO_2 in our simulation will increase the loss of H_2^+, H_3^+ and O_2H^+, through proton transfer as CO_2 has a higher proton affinity than H, H_2, and O_2. However, the newborn ion, HCO_2^+ (45 u q^{-1}), reacts with H_2O to produce H_3O^+: The former ion is a terminal ion in the absence of H_2O and would likely be found over the CO_2 patch when in shadow. In contrast, CO_2^+ from CO_2 ionization is reacting with all other main neutral species either through charge-exchange or hydrogen transfer (e.g. $CO_2^+ + H_2 \longrightarrow HCO_2^+ + H$). Therefore, we do not expect CO_2, CO_2^+, and HCO_2^+ to affect our findings drastically. Nevertheless, CO_2 may be dissociated into C and CO or ionized into C^+ and CO^+: The chemical network becomes more complex owing to C and C^+. The ion-neutral reaction involving C leads to CH^+ and, by cascade effect, to hydrocarbon cations. Mass spectrometers onboard JUICE (S. Barabash et al., in preparation) may be able to detect them. Indeed, even with a limited mass resolution, any signal detected around 12 and 13 u q^{-1} will be unambiguously attributed to resp. C^+ and CH^+ as long as the mass separation is ~ 1 and neglecting isotopologues.

5 CONCLUSION

By including ion-neutral collisions, by means of kinetic rate coefficients, in our kinetic test-particle model, we have tentatively assessed their impact on the ionosphere of an icy moon, with the application here to Ganymede. While ion-neutral chemistry barely affects the total ion number density, except in very specific locations such as the magnetopause, the ion composition, in contrast, is strongly affected, especially near the moon. We show that not only new ion species are produced, namely H_3^+, H_3O^+, and O_2H^+, and others are destroyed, such as H_2^+ and O^+, but also the ion composition significantly depends on the location of the subsolar point with respect to Ganymede's global magnetospheric configuration (which varies with the moon's local time with respect to Jupiter), whether located around the trailing hemisphere (e.g. G07), the leading one, the nearside, or the farside (e.g. G01) of Jupiter.

From a modelling perspective, we provide preliminary results and a simple framework to implement ion-neutral chemistry for computational models, particularly adequate for multi-fluid MHD and hybrid models. As we treat ions as test particles, therefore kinetically, the approach exposed here, described in Appendices A and C combined with a better parametrization of the neutral atmosphere (cf. A. Beth et al. 2025), is the best course of action for those who are interested in accounting for ion-neutral chemistry in their hybrid models (e.g. those of S. Fatemi et al. 2022; A. Stahl et al. 2023) and may compare with our results.

From an observational perspective, this work has strong implications on the future JUICE *in situ* measurements. At the current altitude of the spacecraft orbit (500 or 200 km altitude), we anticipate that JUICE will observe H_2^+, H_3^+, H_3O^+, and O_2^+, the dominant ion species in our simulations. However, we cast doubt on the ability of the JUICE Particle Environment Package (PEP; Barabash et al., in preparation) to separate and distinguish these ions appropriately. Indeed, two PEP sensors are dedicated to ion measurements: Neutral Gas and Ion Mass (NIM) and Jovian Plasma Dynamics and Composition (JDC). While NIM has a sufficient mass resolution ($m/\Delta m \gtrsim 750$), its energy acceptance is limited below 5–10 eV, excluding deceleration/acceleration caused by the spacecraft potential. The lighter the ion species is, the more likely NIM will

Downloaded from https://academic.oup.com/mnras/article/544/1/95/8269935 by Imperial College of Science Technology and Medicine user on 06 November 2025

detect it: a 10 eV H_2^+ goes at 30 km s^{-1} whereas a 10 eV O_2^+ goes at 7 km s^{-1}. A. Beth et al. (2025) showed that a good proxy of the ion velocity based on these MHD simulations is $\vec{E} \times \vec{B}/B^2$. Near the surface at an altitude of $\sim$ 130 km, the location of the inner boundary of the MHD simulation, the ion speed reaches already $\sim$ 10 km s^{-1} depending on the conditions/flybys (cf. fig 12 in A. Beth et al. 2025), such that H_2^+ would be detectable, H_2O^+ maybe (at the detection limit), but not O_2^+. The lowest speeds are found above the magnetic poles, within the cusps, and near the magnetopause such that these locations will be the best places to separate the different water-group ions. In contrast, JDC has an energy acceptance much wider, from 1 eV to 41 keV, but a much lower mass resolution ($m/\Delta m \sim 20$), meaning that water-group ions will be challenging to separate from each other. To interpret the Juno and JUICE ion composition measurements around Ganymede, kinetic models including chemistry, such as the one presented here, are critical.

ACKNOWLEDGEMENTS

AB acknowledges Ronan Modolo for the fruitful interactions and comments on the study. Work at Imperial College London was supported by the Science and Technology Facilities Council (STFC) of the UK under ST/S000364/1 and ST/W001071/1. Test-particle simulations were performed at the Imperial College Computing Service (DOI: 10.14469/hpc/2232). The research performed by FL was funded by the project FACOM (ANR-22-CE49-0005-01 ACT). XJ acknowledges support by the National Aeronautics and Space Administration (NASA) through Early Career Fellow Startup Grant #80NSSC20K1286 and JUICE/PEP contract #183512 with Johns Hopkins University Applied Physics Laboratory. AB acknowledges Fabio Crameri and his scientific colourmaps (used for Figs 2–4) available at 10.5281/zenodo.1243862 and presented in F. Crameri, G. E. Shephard & P. J. Heron (2020).

DATA AVAILABILITY

The data underlying this article will be shared on reasonable request to the corresponding author. MAG (M. Kivelson et al. 2024) and PWS (J. Ansher et al. 2017) data are available on the PDS.

REFERENCES

Adams N., Smith D., 1984, Chem. Phys. Lett., 105, 604
Ajello J. M., Huntress W. T., Lane A. L., LeBreton P. R., Williamson A. D., 1974, J. Chem. Phys., 60, 1211
Allegrini F. et al., 2022, Geophys. Res. Lett., 49, e2022GL098682
Ansher J., Barnhardt B., Richards B., Gurnett D., Kurth W., 2017, NASA Planetary Data System, https://pds-ppi.igpp.ucla.edu/collection/GO-J-PWS-5-DDR-PLASMA-DENSITY-FULL-V1.0
Barth C. A. et al., 1997, Geophys. Res. Lett., 24, 2147
Beth A., Galand M., Modolo R., Jia X., Leblanc F., Huybrighs H. L. F., 2025, MNRAS, 538, 2483
Bockelée-Morvan D. et al., 2024, A&A, 690, L11
Boris J. P., 1970, Proc. Fourth Conf. Num. Sim. Plasmas, 3
Buccino D. R. et al., 2022, Geophys. Res. Lett., 49, e2022GL098420
Carnielli G., Galand M., Leblanc F., Leclercq L., Modolo R., Beth A., Huybrighs H., Jia X., 2019, Icarus, 330, 42
Carnielli G., Galand M., Leblanc F., Modolo R., Beth A., Jia X., 2020a, Icarus, 343, 113691
Carnielli G., Galand M., Leblanc F., Modolo R., Beth A., Jia X., 2020b, Icarus, 351, 113918
Crameri F., Shephard G. E., Heron P. J., 2020, Nature Commun., 11, 5444
Duling S. et al., 2022, Geophys. Res. Lett., 49, e2022GL101688
Eviatar A., M. Vasyliūnas V., A. Gurnett D., 2001, Planet. Space Sci., 49, 327
Fahr H., Müller K. G., 1967, Zeitschrift für Physik, 200, 343
Fatemi S., Poppe A. R., Vorburger A., Lindkvist J., Hamrin M., 2022, J. Geophys. Res. Space Phys., 127, e2021JA029863
Fox J. L., 2015, Icarus, 252, 366
Frank L. A., Ackerson K. L., Lee J. A., English M. R., Pickett G. L., 1992, Space Sci. Rev., 60, 283
Gurnett D. A., Kurth W. S., Shaw R. R., Roux A., Gendrin R., Kennel C. F., Scarf F. L., Shawhan S. D., 1992, Space Sci. Rev., 60, 341
Hall D. T., Feldman P. D., McGrath M. A., Strobel D. F., 1998, ApJ, 499, 475
Hillenbrand P.-M., Ruette N. d., Urbain X., Savin D. W., 2022, ApJ, 927, 47
Huestis D. L., 2008, Planet. Space Sci., 56, 1733
Huntress W. T. J., Pinizzotto R. F. J., 1973, J. Chem. Phys., 59, 4742
Irvine A., Latimer C., 1997, Int. J. Mass Spectr. Ion Process, 164, 115
Jia X., Walker R. J., Kivelson M. G., Khurana K. K., Linker J. A., 2008, J. Geophys. Res. Space Phys., 113, A06212
Jia X., Walker R. J., Kivelson M. G., Khurana K. K., Linker J. A., 2009, J. Geophys. Res. Space Phys., 114, A09209
Johnson R. E., 1990, Energetic charged-particle interactions with atmospheres and surfaces. Physics and Chemistry in Space, Springer Berlin, Heidelberg, https://link.springer.com/book/10.1007/978-3-642-48375-2
Jones J., Birkinshaw K., Twiddy N., 1981, Chem. Phys. Lett., 77, 484
Karpas Z., Anicich V., Huntress W. T. J., 1979, J. Chem. Phys., 70, 2877
Kim J., Theard L., Huntress W., 1974, Int. J. Mass Spectr. Ion Phys., 15, 223
Kim J. K., Huntress W. T. J., 1975, J. Chem. Phys., 62, 2820
Kivelson M., Khurana K., Volwerk M., 2002, Icarus, 157, 507
Kivelson M., Khurana K., Russell C., Walker R., Joy S., Mafi J., 2024, NASA Planetary Data System, https://pds-ppi.igpp.ucla.edu/collection/urn:nasa:pds:galileo-mag-jup-calibrated:data-highres-ganymede
Kivelson M. G. et al., 1996, Nature, 384, 537
Kovalenko A., Tran T. D., Rednyk S., Roućka S., Dohnal P., Plašil R., Gerlich D., Glosík J., 2018, ApJ, 856, 100
Kurth W. S. et al., 2022, Geophys. Res. Lett., 49, e2022GL098591
Leblanc F., Oza A., Leclercq L., Schmidt C., Cassidy T., Modolo R., Chaufray J., Johnson R., 2017, Icarus, 293, 185
Leblanc F. et al., 2023, Icarus, 399, 115557
Marconi M., 2007, Icarus, 190, 155
Millar T. J., Walsh C., Van de Sande M., Markwick A. J., 2024, A&A, 682, A109
Phelps A. V., 1990, J. Phys. Chem. Ref. Data, 19, 653
Plainaki C. et al., 2015, Icarus, 245, 306
Pontoni A., Shimoyama M., Futaana Y., Fatemi S., Poppe A. R., Wieser M., Barabash S., 2022, J. Geophys. Res. Space Phys., 127, e2021JA029439
Prasad S. S., Huntress W. T. Jr, 1980, Astrophys. J. Suppl. Ser., 43, 1
Rakshit A. B., Warneck P., 1980, J. Chem. Soc., Faraday Trans. 2, 76, 1084
Roth L., Ivchenko N., Gladstone G. R., Saur J., Grodent D., Bonfond B., Molyneux P. M., Retherford K. D., 2021, Nat. Astron., 5, 1043
Roth L. et al., 2023, Planet. Sci. J., 4, 12
Saur J. et al., 2015, J. Geophys. Res. Space Phys., 120, 1715
Shematovich V. I., 2008, Solar Syst. Res., 42, 473
Shematovich V. I., 2016, Solar Syst. Res., 50, 262
Smith D., Adams N. G., Miller T. M., 1978, J. Chem. Phys., 69, 308
Smith D., Spanel P., Mayhew C. A., 1992, Int. J. Mass Spectr. Ion Process., 117, 457
Stahl A., Addison P., Simon S., Liuzzo L., 2023, J. Geophys. Res. Space Phys., 128, e2023JA032113
Stancil P. C., Schultz D. R., Kimura M., Gu J.-P., Hirsch G., Buenker R. J., 1999, Astron. Astrophys. Suppl. Ser., 140, 225
Theard L. P., Huntress Wesley T. J., 1974, J. Chem. Phys., 60, 2840
Tran T. D., Rednyk S., Kovalenko A., Roućka S., Dohnal P., Plašil R., Gerlich D., Glosík J., 2018, ApJ, 854, 25
Turner B. R., Rutherford J. A., 1968, J. Geophys. Res. (1896–1977), 73, 6751
Valek P. W. et al., 2022, Geophys. Res. Lett., 49, e2022GL100281
Vasyliūnas V. M., Eviatar A., 2000, Geophys. Res. Lett., 27, 1347
Viggiano A. A., Albritton D. L., Fehsenfeld F. C., Adams N. G., Smith D., Howorka F., 1980, ApJ, 236, 492

Downloaded from https://academic.oup.com/mnras/article/544/1/95/8269935 by Imperial College of Science Technology and Medicine user on 06 November 2025

Vorburger A., Fatemi S., Galli A., Liuzzo L., Poppe A. R., Wurz P., 2022, Icarus, 375, 114810
Vorburger A., Fatemi S., Carberry Mogan S. R., Galli A., Liuzzo L., Poppe A. R., Roth L., Wurz P., 2024, Icarus, 409, 115847
Waite Jr J. H. et al., 2024, J. Geophys. Res. Planets, 129, e2023JE007859
Wakelam V. et al., 2012, ApJS, 199, 21
Weber M. E., Dalleska N. F., Tjelta B. L., Fisher E. R., Armentrout P. B., 1993, J. Chem. Phys., 98, 7855

APPENDIX A: COLLISION SCHEME

We summarize here the different steps in the test-particle including collisions.

Algorithm 1 Ion motion from t to $t + \Delta t$

Ion with position $\vec{x}(t)$ and velocity $\vec{v}(t)$
Locate the ion in the MHD simulation
Interpolate $\vec{E}$ and $\vec{B}$ at position $\vec{x}$ from values $\vec{E}_i$ and $\vec{B}_i$ at the vertices of the MHD cell, associating them a weight w_m
$\vec{E}(\vec{x}) \leftarrow \sum_m^8 w_m \vec{E}_m$
$\vec{B}(\vec{x}) \leftarrow \sum_m^8 w_m \vec{B}_m$
Apply Boris' algorithm to update $\vec{x}$ and $\vec{v}$ from t to $t + \Delta t$
$\vec{v}(t + \Delta t) \overset{\vec{E},\vec{B}}{\leftarrow} \vec{v}(t)$ and $\vec{x}(t + \Delta t) \overset{\vec{E},\vec{B}}{\leftarrow} \vec{x}(t)$
Locate the ion in the exospheric simulation
Derive the ion-neutral collision frequency $\nu_{i,n}$ between the ion species i and the neutral species n based on the neutral density in the exospheric cell
$\nu_{i,n} = \sigma_{i,n}(v_{\rm rel}) v_{\rm rel} n_n$ or $k_{i,n}(T) n_n$
Calculate the collision probability $p_{\rm collision}$ of the ion i with one of the N neutral species n during Δt
$p_{\rm collision} = 1 - \exp(-\sum_n^N \nu_{i,n} \Delta t)$
Draw a random number $p \in \mathcal{U}_{[0,1]}$
if $p < p_{\rm collision}$ **then** ▷ // Ion collides with one neutral species
  Draw a random number $r \in \mathcal{U}_{[0,1]}$
  Initialisation: $p_0 \leftarrow 0$ and $k \leftarrow 0$
  while $p_0 < r$ **do**
    $k \leftarrow k + 1$ ▷ // k: index of the examined neutral species
    $p_k \leftarrow \nu_{i,k} / \sum_n^N \nu_{i,n}$ ▷ // Probability to collide with k
    $p_0 \leftarrow p_0 + p_k$
  end while
  ▷ // Ion species i collides with neutral species k
  ▷ // $A + B^+ \longrightarrow$ products?
  if number of products > 1 **then**
    Draw a random number $s \in \mathcal{U}_{[0,1]}$
    Initialisation: $b_0 \leftarrow 0$ and $l \leftarrow 0$
    while $b_0 < s$ **do**
      $l \leftarrow l + 1$ ▷ // Examining the reaction l
      $b_0 \leftarrow b_0 + b_l$ ▷ // b_l: branching ratio for reaction l
    end while
  ▷ // Ion product j from reaction l
  else
  ▷ // Ion product j from the unique reaction
  end if
  ▷ // The ion i is turned into a new ion j
  Reinitialise the ion properties, mass m and charge q
  $m \leftarrow m_j$ and $q \leftarrow q_j$
  Update $\vec{v}$ following the collision, position $\vec{x}$ is conserved
else
  ▷ // Ion does not collide
end if
Back to 1

We have implemented ion-neutral collision in our test-particle model. As ion–ion interaction is neglected and ions do not have any feedback on the neutral background – which is imposed and maintained in a steady state – a collision between an ion and a neutral species can be easily implemented.

APPENDIX B: KINETIC RATE COEFFICIENT

We provide here the list of ion-neutral reactions from https://umistdatabase.net/ (T. J. Millar et al. 2024). ΔH has been calculated separately. For 'almost' athermic 'reversible' reactions (i.e. $\Delta H \sim \pm 0.01$ eV), namely $H^+ + O \longleftrightarrow H + O^+$ and $O_2H^+ + H_2 \longleftrightarrow O_2 + H_3^+$, we set ΔH to 0. The rate coefficient is given by

$$k_{in}(T)[10^{-10}\mathrm{cm^3\,s^{-1}}] = \alpha \left(\frac{T}{300}\right)^{\beta} \exp(-\gamma/T) \tag{B1}$$

with α, β, and γ are tabulated in Table B1. The absence of values corresponds to 0.6

APPENDIX C: UPDATING ION VELOCITY POST-COLLISION

After an ion-neutral collision, the ion product from the reaction has a new velocity that should be calculated based on the initial properties of the reactants. In addition, as discussed in Appendix B, the ion-neutral collisions considered here are a priori exothermic (spontaneous in the gas phase). In reality, some reactions are only triggered above a certain energy threshold (hence endothermic) when collisions are treated from a pure kinetic aspect involving the energy-dependent cross-sections that are ignored here. As they are exothermic, the excess energy of the reaction should be redistributed: It is mainly dissipated through excitation and change in the kinetic energy of the products. We assume no excitation of the products as they are no data to support our modelling here. To determine the post-collision ion velocity, we assume that the excess energy ΔH is redistributed into kinetic energy only. Our approach is considered quasi-elastic. Assuming energy conservation before and after the collisions, one gets

$$\frac{1}{2}m_1 v_1^2 + \frac{1}{2}m_2 v_2^2 = \frac{1}{2}m_3 v_3^2 + \frac{1}{2}m_4 v_4^2 - \Delta H, \tag{C1}$$

where ΔH is the excess energy ($\Delta H > 0$ for exothermic reactions), $\vec{v}_s$ is the velocity of the species s (products or reactants), and m_s is their mass. We assume that the centre of mass velocity is conserved $\vec{v}_{\rm CM}$, as no external force is applied to the system during the collision, given by

$$\vec{v}_{\rm CM} = \frac{m_1\vec{v}_1 + m_2\vec{v}_2}{m_1 + m_2} = \frac{m_3\vec{v}_3 + m_4\vec{v}_4}{m_3 + m_4}. \tag{C2}$$

We define $\vec{u}_s$ as the velocity in the centre of mass frame such that $\vec{v}_s = \vec{v}_{\rm CM} + \vec{u}_s$. In the centre of mass frame $m_1\vec{u}_1 = -m_2\vec{u}_2$ and $m_3\vec{u}_3 = -m_4\vec{u}_4$. In addition, there is no change in mass, $m_1 + m_2 = m_3 +$

Downloaded from https://academic.oup.com/mnras/article/544/1/95/8269935 by Imperial College of Science Technology and Medicine user on 06 November 2025

Table B1. List of ion-neutral reactions for our test-particle model. Values for α [10^{-16} m^{-3} s^{-1}], β, and γ are taken from https://umistdatabase.net/. ΔH is the excess energy associated with each reaction, n° refers to the reaction's number on the website. References to the relevant publications are given.

							α	β	γ	ΔH	n°	References
H^+	+	H	⟶	$h\nu$	+	H_2^+		N/A				
	+	H_2	⟶	None								
	+	O	⟶	H	+	O^+	6.86	0.26	224.3	0	417	P. C. Stancil et al. (1999)
	+	HO	⟶	H	+	HO^+	21	−0.50		0.58	419	S. S. Prasad & W. T. Huntress (1980)
	+	H_2O	⟶	H	+	H_2O^+	69	−0.50		0.98	388	D. Smith, P. Spanel & C. A. Mayhew (1992)
	+	O_2	⟶	H	+	O_2^+	20			1.53	416	D. Smith et al. (1992)
H_2^+	+	H	⟶	H_2	+	H^+	6.4			1.83	500	Z. Karpas, V. Anicich & J. Huntress (1979)
	+	H_2	⟶	H	+	H_3^+	20.8			1.68	3189	L. P. Theard & J. Huntress (1974)
	+	O	⟶	H	+	HO^+	15			2.34	3201	S. S. Prasad & W. T. Huntress (1980)
	+	HO	⟶	H_2	+	HO^+	7.6	−0.50		2.41	467	S. S. Prasad & W. T. Huntress (1980)
			⟶	H	+	H_2O^+	7.6	−0.50		3.43	3202	S. S. Prasad & W. T. Huntress (1980)
	+	H_2O	⟶	H_2	+	H_2O^+	39	−0.50		2.80	458	J. K. Kim & J. Huntress (1975)
			⟶	H	+	H_3O^+	34	−0.50		4.43	3191	J. K. Kim & J. Huntress (1975)
	+	O_2	⟶	H_2	+	O_2^+	8			3.36	466	J. K. Kim & J. Huntress (1975)
			⟶	H	+	O_2H^+	19			1.67	3200	J. K. Kim & J. Huntress (1975)
H_3^+	+	H	⟶	None								
	+	H_2	⟶	None								
	+	O	⟶	H_2	+	HO^+	4.65	−0.14	0.67	1.69	3548	P.-M. Hillenbrand et al. (2022)
			⟶	H	+	H_2O^+	2.08	−0.40	4.86	0.66	3547	P.-M. Hillenbrand et al. (2022)
	+	HO	⟶	H_2	+	H_2O^+	13	−0.50		1.75	3550	S. S. Prasad & W. T. Huntress (1980)
	+	H_2O	⟶	H_2	+	H_3O^+	59	−0.50		2.75	3499	J. Kim, L. Theard & W. Huntress (1974)
	+	O_2	⟶	H_2	+	O_2H^+	9.3		100	0	3546	N. Adams & D. Smith (1984)
O^+	+	H	⟶	O	+	H^+	5.66	0.36	−8.6	0	503	Z. Karpas et al. (1979)
	+	H_2	⟶	H	+	HO^+	13.5			0.53	3274	A. Kovalenko et al. (2018)
	+	O	⟶	Sym.								
	+	HO	⟶	O	+	HO^+	3.6	−0.50		0.60	675	S. S. Prasad & W. T. Huntress (1980)
			⟶	H	+	O_2^+	3.6	−0.50		2.25	4536	S. S. Prasad & W. T. Huntress (1980)
	+	H_2O	⟶	O	+	H_2O^+	32	−0.50		1.00	667	D. Smith, N. G. Adams & T. M. Miller (1978)
	+	O_2	⟶	O	+	O_2^+	0.19			1.55	673	D. Smith et al. (1978)
HO^+	+	H	⟶	None								
	+	H_2	⟶	H	+	H_2O^+	12.7	0.18		1.02	3277	T. D. Tran et al. (2018)
	+	O	⟶	H	+	O_2^+	7.1			1.65	4638	S. S. Prasad & W. T. Huntress (1980)
	+	HO	⟶	O	+	H_2O^+	7	−0.50		1.09	4676	S. S. Prasad & W. T. Huntress (1980)
	+	H_2O	⟶	HO	+	H_2O^+	15.9	−0.50		0.40	700	J. Huntress & J. Pinizzotto (1973)
			⟶	O	+	H_3O^+	13	−0.50		2.10	4667	J. Huntress & J. Pinizzotto (1973)
	+	O_2	⟶	HO	+	O_2^+	5.9			0.95	705	J. Jones, K. Birkinshaw & N. Twiddy (1981)
H_2O^+	+	H	⟶	None								
	+	H_2	⟶	H	+	H_3O^+	9.7			1.62	3250	T. D. Tran et al. (2018)
	+	O	⟶	H_2	+	O_2^+	0.4			0.63	4621	A. A. Viggiano et al. (1980)
	+	HO	⟶	O	+	H_3O^+	6.9	−0.50		1.69	4687	S. S. Prasad & W. T. Huntress (1980)
	+	H_2O	⟶	HO	+	H_3O^+	21	−0.50		1.00	3317	J. Huntress & J. Pinizzotto (1973)
	+	O_2	⟶	H_2O	+	O_2^+	4.6			0.55	485	A. B. Rakshit & P. Warneck (1980)
H_3O^+	+	H	⟶	None								
	+	H_2	⟶	None								
	+	O	⟶	None								
	+	HO	⟶	None								
	+	H_2O	⟶	None								
	+	O_2	⟶	None								
O_2^+	+	H	⟶	None								
	+	H_2	⟶	None								
	+	O	⟶	None								
	+	HO	⟶	None								
	+	H_2O	⟶	None								
	+	O_2	⟶	Sym.								
O_2H^+	+	H	⟶	None								
	+	H_2	⟶	O_2	+	H_3^+	6.4			0	3276	N. Adams & D. Smith (1984)
	+	O	⟶	O_2	+	HO^+	6.2			0.67	4637	S. S. Prasad & W. T. Huntress (1980)
	+	HO	⟶	O_2	+	H_2O^+	6.1	−0.50		1.76	4694	S. S. Prasad & W. T. Huntress (1980)
	+	H_2O	⟶	O_2	+	H_3O^+	8.2	−0.50		2.76	3369	S. S. Prasad & W. T. Huntress (1980)
	+	O_2	⟶	None								

Downloaded from https://academic.oup.com/mnras/article/544/1/95/8269935 by Imperial College of Science Technology and Medicine user on 06 November 2025

$m_4 = M$. From equation (C1),

$$\begin{aligned}
m_1 v_1^2 + m_2 v_2^2 &= m_3 \|\vec{v}_{\rm CM} + \vec{u}_3\|^2 + m_4 \|\vec{v}_{\rm CM} + \vec{u}_4\|^2 - 2\Delta H \\
m_1 v_1^2 + m_2 v_2^2 &= M v_{\rm CM}^2 + m_3 u_3^2 + m_4 u_4^2 - 2\Delta H \\
\frac{(m_1+m_2)}{M}(m_1 v_1^2 + m_2 v_2^2) &= \frac{\|m_1\vec{v}_1 + m_2\vec{v}_2\|^2}{M} + m_3 u_3^2 + \underbrace{m_4 u_4^2}_{m_3^2 u_3^2/m_4} - 2\Delta H \\
&= \frac{m_1^2 v_1^2 + 2\vec{v}_1\cdot\vec{v}_2 + m_2^2 v_2^2}{M} \\
&\quad + \left(m_3 + \frac{m_3^2}{m_4}\right) u_3^2 - 2\Delta H \\
\frac{m_1 m_2}{M}(v_1^2 - 2\vec{v}_1\cdot\vec{v}_2 + v_2^2) &= \frac{M}{m_4} m_3 u_3^2 - 2\Delta H \\
\overbrace{\frac{m_1 m_2}{M}\|\underbrace{\vec{v}_1 - \vec{v}_2}_{\vec{v}_{\rm rel.}}\|^2}^{2E_{\rm rel.}} &= \frac{M}{m_4} m_3 u_3^2 - 2\Delta H \\
u_3^2 &= \frac{m_4}{m_3 M}(2E_{\rm rel.} + 2\Delta H)
\end{aligned}$$

such that

$$u_3^2 = \left[\frac{2m_4}{m_3 M}\right](E_{\rm rel.} + \Delta H)$$

$$u_4^2 = \left[\frac{2m_3}{m_4 M}\right](E_{\rm rel.} + \Delta H)$$

where $E_{\rm rel.} = \mu\|\vec{v}_1 - \vec{v}_2\|^2/2$ is by definition the total kinetic energy in the centre of mass frame and $\mu = m_1 m_2/M$ is the reduced mass before the collision and is conserved during charge exchange reactions, unlike proton transfer. The result is consistent with endothermic reactions only triggered above a certain relative speed (with the condition $E_{\rm rel.} > \Delta H$ or $\|\vec{v}_1 - \vec{v}_2\| > \sqrt{2\Delta H/\mu}$). As ΔH is usually provided in eV and mass in u (or Da), a useful conversion is 1 J kg $= 9.65 \times 10^7$ eV u.

The new velocity is then $\vec{v}_3 = \vec{v}_{\rm CM} + u_3\vec{U}$ where $\vec{U}$ is a random vector of norm 1 equivalent at drawing a random point on a sphere centred on 0 of radius 1. Note that in the low relative speed limit ($\|\vec{v}_1 - \vec{v}_2\| \approx 0$), $u_3 = \sqrt{m_4/m_3}\sqrt{2\Delta H/M}$. This shows that an ion-neutral reaction such as $H_2O + H_2O^+ \longrightarrow HO + H_3O^+ + 1$ eV (cf. Appendix C) in slow relative speed limit releases H_3O^+ above 2 km s^{-1}.

This also showed that a priori ions should be a mix of several populations with different temperatures. For instance, H_3O^+ is formed through different reactions with different ΔH from 1.00 eV to 4.43 eV. However, H_3O^+ is often the most massive of the products; hence, it recoups less than half of this energy. For example, in the low relative velocity limit, for $H_2O + H_2O^+$, 0.47 eV would be given to H_3O^+. However, for $H_2^+ + H_2O$, although the reaction is the most energetic, H_3O^+ gets back 0.22 eV only.

APPENDIX D: MOLECULAR PROPERTIES

Proton affinities and ionization energies of the different neutral species are listed in Table D1. As H has the lowest proton affinity (PA), H_2^+ reacts with all neutrals to transfer one proton. In contrast, having the highest PA, H_2O steals a proton from any protonated molecule. As H_2 and O_2 have extremely close PA, the proton transfer reaction is almost athermic and therefore reversible. Similar analysis can be done by looking at the ionization energy. On the one hand, O_2 has the lowest ionization energy (IE) in the ground state. Therefore, O_2^+ is unlikely to be neutralized through charge exchange (except with O_2). Nevertheless, O_2^+ can react with neutral species if it is in an excited state. On the other hand, H_2 has the largest ionization energy, leading to the neutralization of H_2^+. Having both a large IE and a low PA is why H_2^+ may often lead to two different ion products by reacting with one given neutral species as it will easily either capture an electron or transfer its proton. O^+ with the second highest IE (though close to that of H^+) makes it very reactive through charge exchange, leading to its loss. By a simple analysis, it is already possible to anticipate the main ion species: H_3O^+ based on PA and O_2^+ based on IE.

The priority order for both processes are as follows:

(i) PA: H_2^+, O_2H^+, H_3^+, HO^+, H_2O^+, H_3O^+ (you tend to form the latter following successive proton transfer)
(ii) IE: H_2^+, O^+, H^+, HO^+, H_2O^+, O_2^+ (you tend to form the latter following successive charge-exchange)

Table D1. Proton affinity (PA) and ionization energy (IE) of the different neutral species detected at Ganymede.

Species	PA (eV)	IE (eV)
H	2.67	13.598
H_2	4.38	15.425
O	5.03	13.618
HO	6.15	13.017
H_2O	7.16	12.621
O_2	4.37	12.070

Downloaded from https://academic.oup.com/mnras/article/544/1/95/8269935 by Imperial College of Science Technology and Medicine user on 06 November 2025

O^+ and H^+ are not involved in proton transfer reactions, while H_3^+, H_3O^+, and O_2H^+ are not in charge-exchange ones.

APPENDIX E: ENERGY SPECTRA

For completeness, we have simulated similar energy spectra than those in A. Beth et al. (2025) for G01, G07, and G29 flybys, including ion-neutral collisions. Fig. E1 should be compared with Fig. 7 in A. Beth et al. (2025): Except being slightly noisier owing to fewer macroparticles, the spectra do not exhibit noticeable differences. Although we have simulated new ions namely H_3^+, H_3O^+, and O_2H^+, their mass is not drastically different from those already simulated in the collisionless case: $m_{H_3^+}/m_{H_2^+} = 1.5$, $m_{H_3O^+}/m_{H_2O^+} = 1.06$, and $m_{O_2H^+}/m_{O_2^+} = 1.03$. In addition, as ions already spread over several energy bins, H_3^+ ion energy blends with that of H_2^+, H_3O^+ with $H_2O^+/HO^+/H^+$, and O_2H^+ with O_2^+.

Downloaded from https://academic.oup.com/mnras/article/544/1/95/8269935 by Imperial College of Science Technology and Medicine user on 06 November 2025

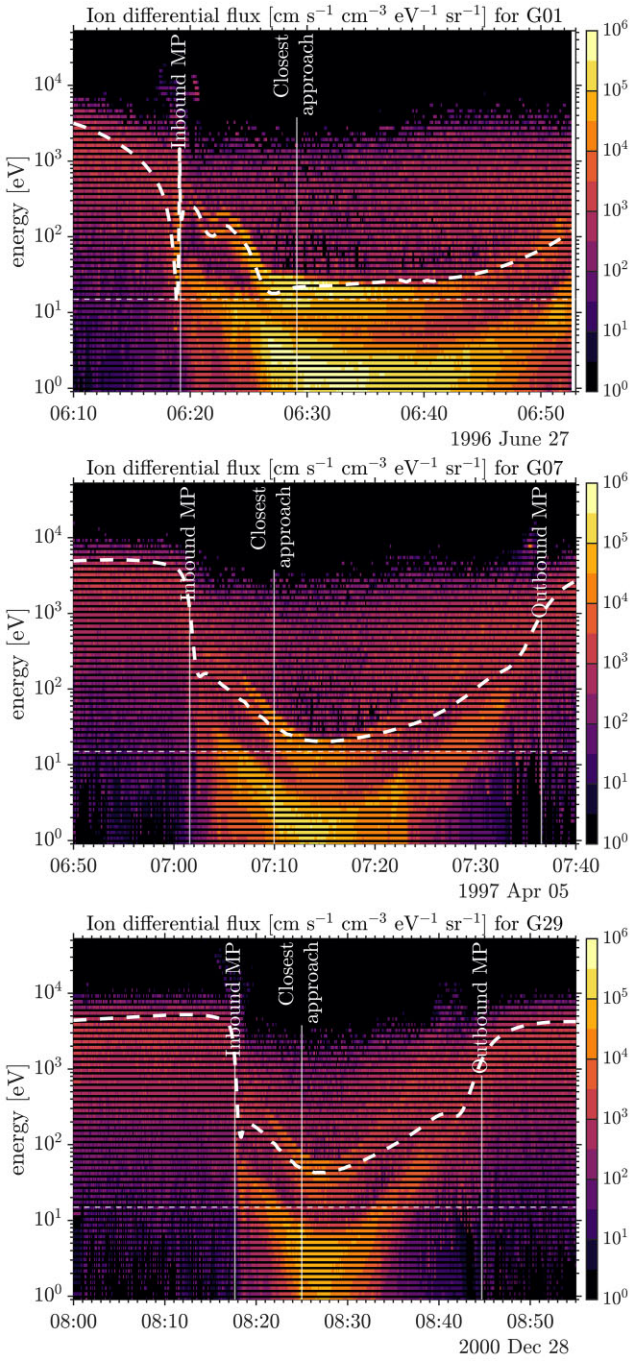


Figure E1. Simulated ion energy spectra as a function of time for G01 (left), G07 (middle), and G29 (right) flybys with ion-neutral chemistry. The white dashed line is the kinetic energy of an O_2^+ drifting at the local $\|\vec{E} \times \vec{B}\|/B^2$ speed in the spacecraft frame. To be compared with fig. 7 from A. Beth et al. (2025).

This paper has been typeset from a TEX/LATEX file prepared by the author.

Downloaded from https://academic.oup.com/mnras/article/544/1/95/8269935 by Imperial College of Science Technology and Medicine user on 06 November 2025

© The Author(s) 2025.
Published by Oxford University Press on behalf of Royal Astronomical Society. This is an Open Access article distributed under the terms of the Creative Commons Attribution License (https://creativecommons.org/licenses/by/4.0/), which permits unrestricted reuse, distribution, and reproduction in any medium, provided the original work is properly cited.